Topology of the redox network during induction of photosynthesis as revealed by time-resolved proteomics in tobacco

David Zimmer, Corné Swart, Alexander Graf, Stéphanie Arrivault, Michael Tillich, Sebastian Proost, Zoran Nikoloski, Mark Stitt, Ralph Bock, Timo Mühlhaus, et al.

PLANT SCIENCES

Topology of the redox network during induction of photosynthesis as revealed by time-resolved proteomics in tobacco

David Zimmer[1], Corné Swart[2], Alexander Graf[2], Stéphanie Arrivault[2], Michael Tillich[2], Sebastian Proost[2]†‡, Zoran Nikoloski[2,3], Mark Stitt[2], Ralph Bock[2], Timo Mühlhaus[1]*, Alix Boulouis[2,4]*

Photosynthetically produced electrons provide energy for various metabolic pathways, including carbon reduction. Four Calvin-Benson cycle enzymes and several other plastid proteins are activated in the light by reduction of specific cysteines via thioredoxins, a family of electron transporters operating in redox regulation networks. How does this network link the photosynthetic chain with cellular metabolism? Using a time-resolved redox proteomic method, we have investigated the redox network in vivo during the dark–to–low light transition. We show that redox states of some thioredoxins follow the photosynthetic linear electron transport rate. While some redox targets have kinetics compatible with an equilibrium with one thioredoxin (TRXf), reduction of other proteins shows specific kinetic limitations, allowing fine-tuning of each redox-regulated step of chloroplast metabolism. We identified five new redox-regulated proteins, including proteins involved in Mg^{2+} transport and $^1O_2$ signaling. Our results provide a system-level functional view of the photosynthetic redox regulation network.

INTRODUCTION

In nature, plants generally experience a dark-to-light transition every 24 hours. A large range of concomitant metabolic, gene expression, and signaling events allow plant cells to start the day. In the chloroplast stroma, adenosine 5′-triphosphate (ATP) and reducing equivalents produced by photosynthesis allow the activation of carbon fixation and inorganic nitrogen assimilation, while starch degradation stops (*1*). Photosynthesis products are exported out of the chloroplast by the triose-phosphate/phosphate shuttle (*2*) and the malate-oxaloacetate valve (*3*), and chloroplast translation is activated (*4*). The circadian clock participates in the regulation of these processes, allowing cellular processes to synchronize with day-night cycles (*5*). However, most of these changes are directly controlled by light, as evidenced by their occurrence even in an out-of-cycle dark-to-light transition.

In the chloroplast photosynthetic system, electrons generated by photosystem I (PSI) enter the stromal compartment, where they can be used to drive different pathways. Apart from carbon reduction and redox regulation, electrons (i) are used to reduce nitrogen and sulfur, (ii) generate reactive oxygen species, (iii) can cycle back to water or reenter the thylakoid electron transfer chain via cyclic electron flow, or (iv) are exported out of the chloroplast to serve metabolism in other compartments. The proportions of electrons distributed to the different routes vary greatly depending on physiological needs and environmental conditions. The factors involved in the regulation of this distribution are currently the subject of intense research [e.g., (*3*, *6*, *7*)]. In theory, redox reactions using electrons from photosynthesis can be controlled by two types of factors: thermodynamics, where the redox states of the reaction partners are determined by their redox potentials, or kinetic constraints that prevent the establishment of equilibrium by slowing down the reaction. Most biological redox reactions are displaced from equilibrium (*8*) because of various constraints, including low enzyme abundance and slow catalysis rates, formation of protein supercomplexes and microcompartments, and, as demonstrated by in vitro studies, regulation of redox potentials (*6*, *8*, *9*).

Since the 1960s, dark-to-light kinetics of activation or deactivation of the light-dependent metabolic processes have been measured with enzyme activity assays. For the Calvin-Benson cycle (CBC), the main pathway of carbon fixation in the chloroplast, kinetics have been obtained for five enzymes: glyceraldehyde-3-phosphate dehydrogenase (GAPDH), ribulose-1,5-bisphosphate carboxylase oxygenase (Rubisco), chloroplast fructose-1,6-bisphosphatase (cpFBPase), sedoheptulose-1,7-bisphosphatase (SBPase), and phosphoribulokinase (PRK) (*10*–*13*). Various factors influencing these kinetics have been identified, including stromal pH, the concentrations of Mg^{2+}, substrate and/or product, redox and phosphorylation states of the enzymes, and engagement of the enzymes in multiprotein complexes (*14*). While most redox-regulated enzymes are activated in the light by cysteine reduction, glucose-6-phosphate dehydrogenase (G6PDH) is an exception, being activated by cysteine oxidation in the dark (*15*). Dark-to-light kinetics of the redox states of some enzymes were also recorded using immunoblot-based techniques (*16*–*19*).

The physiology of the redox regulation network in plant cells is just starting to be unveiled. In the chloroplast, electrons can reach the redox regulators, thioredoxins (TRXs) and reduced form of nicotinamide adenine dinucleotide (NAD^+) phosphate (NADPH)–TRX reductase C (NTRC), via two different routes: a photosynthetic one via ferredoxin and a nonphotosynthetic one for NTRC via the oxidative pentose phosphate pathway (*20*). After a dark-to-light transition, the redox regulators reduce targets until a steady state is reached, a process that depends on light intensity (*21*). Targets are reoxidized by a genetically identified system involving TRXs, 2-Cys

[1]Computational Systems Biology, TU Kaiserslautern, 67663 Kaiserslautern, Germany. [2]Max Planck Institute of Molecular Plant Physiology, Am Muehlenberg 1, D-14476 Potsdam-Golm, Germany. [3]Bioinformatics, Institute of Biochemistry and Biology, University of Potsdam, 14476 Potsdam-Golm, Germany. [4]Laboratory of Chloroplast Biology and Light-sensing in Microalgae, UMR7141, CNRS, Sorbonne Université, Institut de Biologie Physico-Chimique, 75005 Paris, France.
*Corresponding author. Email: boulouis@ibpc.fr (A.B.); muehlhaus@bio.uni-kl.de (T.M.)
†Present address: Laboratory of Molecular Bacteriology, Department of Microbiology and Immunology, Rega Institute, KU Leuven, 3000 Leuven, Belgium.
‡Present address: Center for Microbiology, VIB, 3000 Leuven, Belgium.

peroxiredoxins (2-Cys PRXs), H_2O_2, and NTRC, which together facilitate return to an oxidized state in the dark (*22*–*24*). There are many chloroplast TRXs, the precise number depending on the plant species (table S1) (*20*). Members of the TRX protein family have been shown in vitro to reduce different targets with different specificities, although TRXf stands out as an efficient generalist reducer (*25*). About 20 TRX targets are known to undergo redox regulation in vivo (*26*), compared to over a thousand potential targets identified in vitro in redox proteomic studies (table S2). Most in vivo identified TRX targets are located in the chloroplast, and some have been found in the mitochondrion and the cytosol (*26*). The latter two compartments contain the complete set of actors (TRX, NTR, PRX, and glutaredoxins) for redox regulation, although reducing power is solely provided by NAD(P)H, a fundamental difference compared with the chloroplast (table S1) (*27*, *28*). The interactions between the redox networks of different compartments rely on transporters and redox exchange systems such as the malate valves (*3*, *29*). Our current knowledge on the different redox network components and on network function was mainly inferred from mutant analysis and in vitro studies. What has been missing is the simultaneous in vivo recording of the redox states of TRXs and their targets, and the correlation of these states with the biochemical activities of the target proteins in wild-type plants and under physiological conditions.

Here, we report a time-resolved redox proteomic study during the dark-to-light transition in wild-type tobacco (*Nicotiana tabacum*) plants. We used a transition from darkness to low light for several reasons. First, it ensures that the redox network is not fully saturated with electrons. The latter might mask kinetic limitations that become more obvious in low light. Second, low light mimics the dawn transition in natural light regimes far better than an abrupt transition from darkness to high light. Third, tight regulation of redox activation may be especially important in low light to minimize wasteful futile cycles. By assessing the thermodynamic parameters of the reduction reactions between TRXf and its identified target proteins, our data provide a system-level analysis of the chloroplast redox network. In addition, by measuring photosynthetic parameters and metabolite levels, we obtained insight into not only electron entry into the redox network but also its effects on target activities in vivo. Last, we identified five new redox-regulated chloroplast proteins, thus broadening the landscape of redox-regulated processes in the chloroplast. Together, our datasets provide an extensive characterization of the activation of chloroplast metabolism upon dark-to-light transition.

RESULTS

A set of chloroplast proteins, one mitochondrial protein, and one nucleocytosolic protein change redox states upon dark-to-light transition

To characterize the redox changes occurring in tobacco plants upon dark-to-light transition, a workflow based on differential labeling of cysteine residues and subsequent protein identification by mass spectrometry (MS)–based proteomics was developed (Fig. 1, A to C). As described in Materials and Methods and summarized in Fig. 1, A to C, oxidized forms of the proteins are specifically S-derivatized with polyethylene glycol (PEG)–maleimide, acquiring an additional 10 kDa. This mass increase enables separation by SDS–polyacrylamide gel electrophoresis into two redox clusters representing the oxidized and reduced forms of the proteins. The total abundance of a redox-regulated protein (in the non-PEGylated control sample) and the reduced form of the protein are therefore measured in the same gel fraction(s), allowing the determination of the percentage of reduced protein at each time point (Fig. 1, B and C, and data files S1 to S3).

We partitioned the proteins into three classes based on how their redox state changes during the induction of photosynthesis (Fig. 1D and data files S1 and S2): (i) light-responsive proteins with oxidized cysteines in the dark, whose redox states change after illumination (Fig. 2, Table 1, and data file S3), (ii) proteins with cysteines that are oxidized in the dark and remain oxidized in the light (data file S3), and (iii) proteins that have no cysteines, whose cysteines are always reduced or whose redox behavior is not detected in our experimental setup. Of 1695 measured proteins, 104 (6%) have oxidized cysteine(s) in the dark, and of these, 27 (2% of the total set) show redox changes upon illumination (Fig. 1D).

As expected, chloroplast proteins are strongly represented in the "Oxidized Cys" and "Light-responsive" subsets of proteins (Fig. 1D). Chloroplast proteins are the largest group of oxidized proteins in the dark (42 of 104 proteins), representing 7% of the 635 detected proteins predicted to be in the plastid. Chloroplast localization also ranks first for proteins with a redox change in the light (with 20 proteins, representing nearly half of the oxidized chloroplast proteins). Among these 20 proteins, 12 have both reduced and oxidized clusters (see Materials and Methods) that significantly change compared to darkness (Tables 1 and 2 and data file S3). These include not only well-known redox-related proteins [PRK, SBPase, subunit B of GAPDH (GAPB), subunit gamma of ATP synthase (ATPC1), TRXs TRXf and chloroplastic drought-induced stress protein of 32 kD (CDSP32), proton gradient regulator 5-like 1 (PGRL1), NADP–malate dehydrogenase (NADP-MDH), and 2-carboxy-D-arabinitol-1-bisphosphate phosphatase (CA1Pase)] but also proteins for which a redox regulation was not previously known, such as the Mg^{2+} transporter MGT10/MRS2-11, the putative translation elongation factor suppressor of variegation 3 (SVR3), and conserved in the green lineage 52 (CGL52), a protein with yet unknown function. The lipoamide dehydrogenase subunit of the pyruvate decarboxylase complex (PDC-E3) was also found to undergo redox changes, which correspond to known modifications in enzyme activity (*30*). Chloroplast-localized proteins with only one significant cluster include G6PDH (G6PD1) and the small subunit of adenosine 5′-diphosphate (ADP)–glucose pyrophosphorylase (APS1), two well-known redox-regulated proteins, and a putative methyltransferase with unknown substrate specificity (PPKMT1/SAFE1), which has not been shown to be redox-regulated. All of the identified chloroplast proteins whose redox states changed over time are nucleus-encoded. The kinetics recorded are as diverse as they could be in a four-point time series, with examples of reduction starting before 0.5, 1.7, or 10 min of light, reaching the fully reduced state at 0.5 or 1.7 min or continuing beyond 1.7 min. In some cases, reduction was transient, as for PGRL1, PDC-E3, TRXf, CDSP32, NADP-MDH, and cpFBPase 2 (Fig. 2).

Among proteins with nonchloroplast localizations, extracellular proteins show the highest enrichment in the Oxidized Cys set, corresponding to 31 of 85 proteins with predicted extracellular localization. This was to be expected, given that the extracellular environment is more oxidizing than the intracellular milieu. Five extracellular proteins are present in the light-responsive subset (Tables 1 and 2). Their redox changes are due to variations in their oxidized clusters, sometimes increasing above the level of oxidized protein observed in darkness. These changes are never accompanied by a

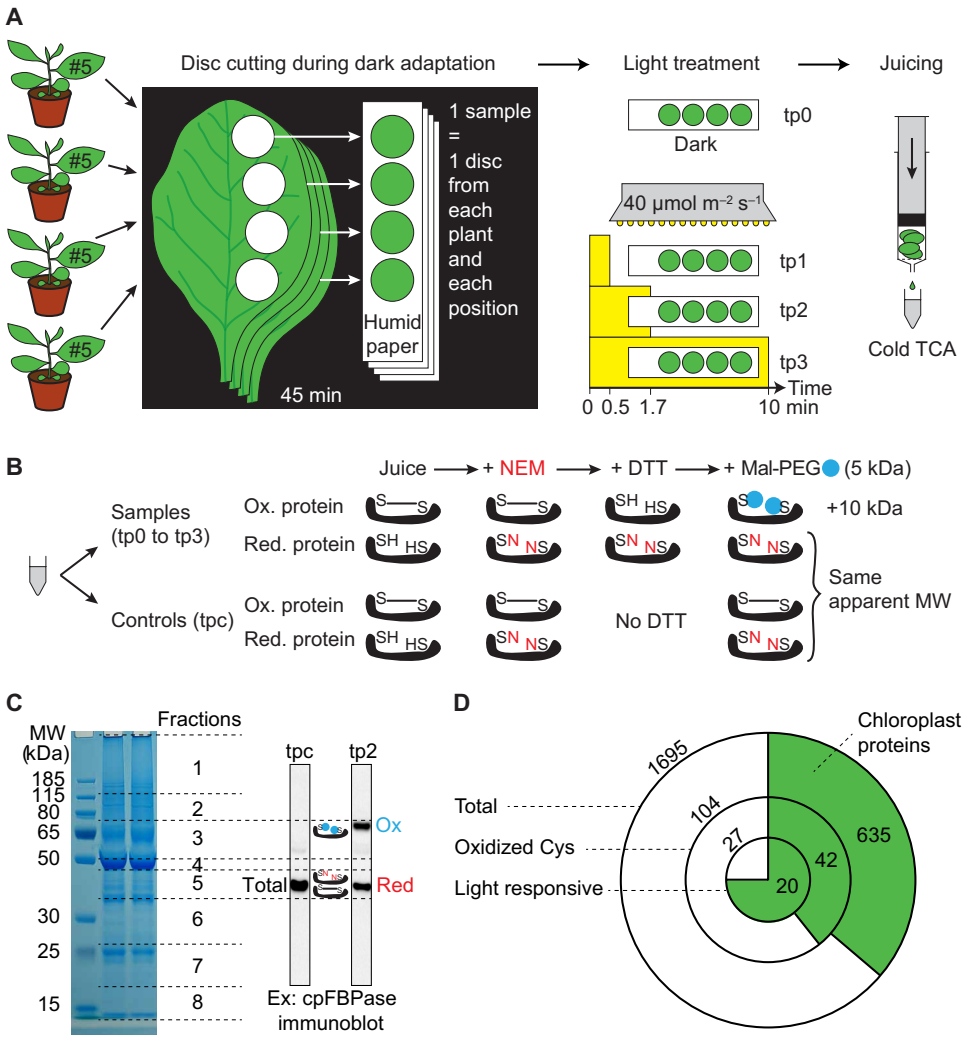

Fig. 1. Overview of the redox proteomic method and findings based on its application on photosynthesis induction in tobacco. (**A**) Sample collection. Each replicate comprises leaf #5 of four plants. The light applied for the different illumination times is the same as the growth light. tp, time point; TCA, trichloroacetic acid. (**B**) Differential labeling of the cysteines in the samples (tp0 to tp3) and the corresponding controls (tpc) using the two alkylating agents *N*-ethyl-maleimide (NEM; or N in the schematic representation of the proteins) and PEGylated maleimide (Mal-PEG; or blue circle in the schematic representation of the proteins). This labeling method distinguishes reduced cysteines (SH) from all dithiothreitol (DTT)–reversible oxidized forms (including disulfide bridges; S-S). MW, molecular weight. (**C**) Fractions of gels cut for MS analysis and validation of the labeling protocol by cpFBPase immunoblots (for immunoblots for all samples of the three replicates, see fig. S1). (**D**) Summary of the results after data analysis. The outer circle representing all measured proteins is not drawn to scale. Numbers outside the circles show the total numbers of measured proteins in the three classes. Chloroplast proteins are indicated with numbers in the green areas.

corresponding change in the reduced clusters, suggesting that they are not due to a change of the redox state but rather a change in total protein abundance. It cannot be excluded that synthesis or degradation of extracellular oxidized proteins could be linked to a wounding response in our experimental system (from disc cutting; Fig. 1A) (*31*); however, the low light intensity and short experimental time used in this study are not expected to cause relevant systemic oxidative stress. Most other subcellular localizations are underrepresented in the light-responsive subset, with only one mitochondrial (i.e., PRXIIF) protein and one nuclear/cytosolic (i.e., NRX1) protein showing changes in their oxidized clusters. These two proteins belong to the redox regulation systems of their compartments and undergo oxidation in the light, opposite to what is seen in chloroplast proteins. Both of the detected cytosolic TRXs (i.e., NRX1 and TRXh; POT001047_1 in data file S3) are more reduced in darkness (~55 and ~70%, respectively) than the chloroplast TRXs (~0%). This different behavior reflects the activity of darkness metabolism in the different compartments, with cytosolic glycolysis and the oxidative pentose-phosphate pathway (OPPP) being active in darkness and producing reducing power, while in the chloroplast, photosynthesis is inactive and starch degradation and OPPP probably have lowered activity after only 45 min of darkness (*32*). To obtain an integrated view of the physiological adaptations occurring upon dark-to-light transition, we next compared the observed redox kinetics with photosynthetic and metabolite measurements.

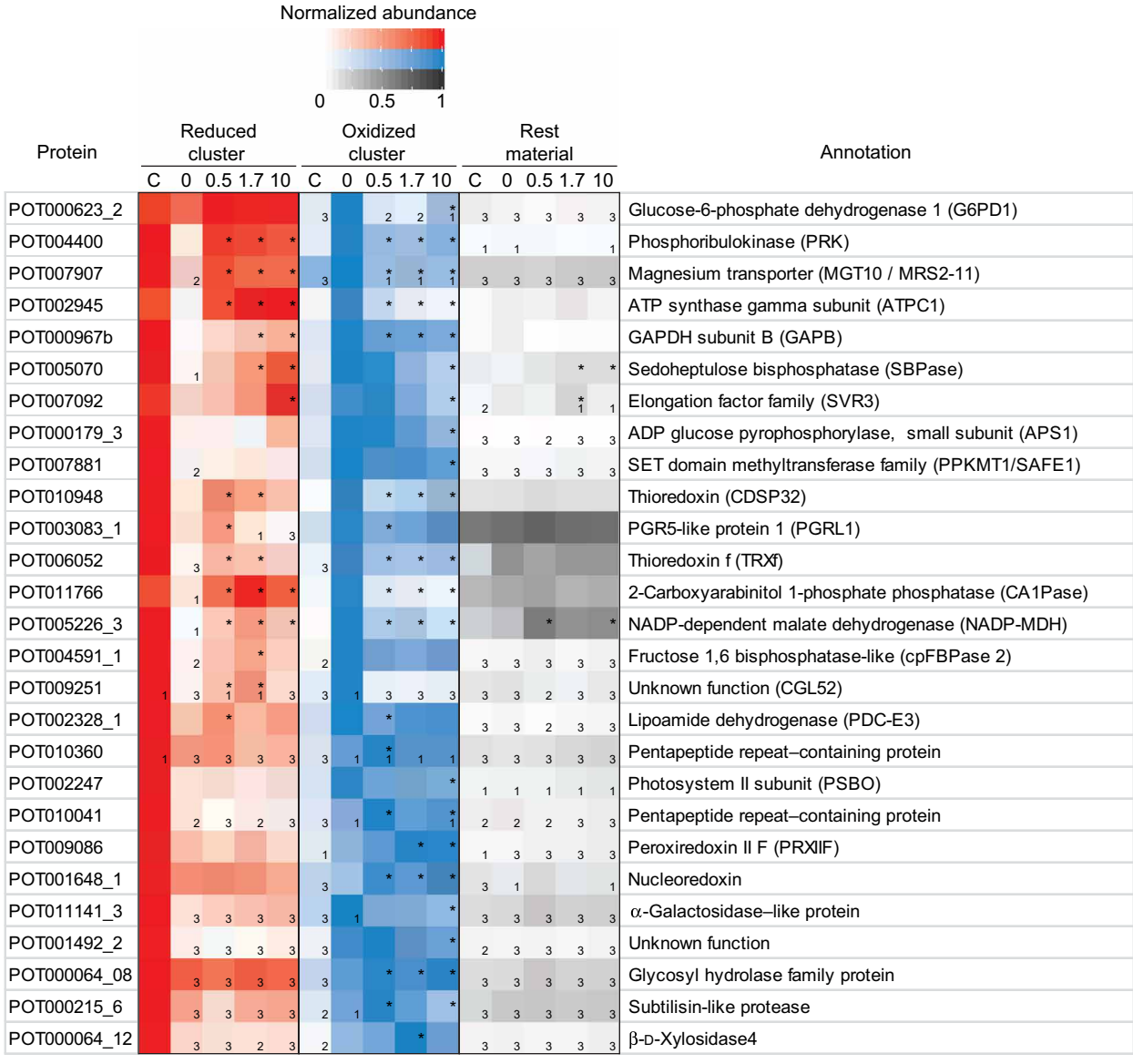

Fig. 2. Redox proteomic data for the 27 proteins whose redox states change with time after dark-to-light transition. Heatmaps of the reduced and oxidized clusters and the rest material (averaged over the three replicates) are presented. Each of the reduced and oxidized clusters was normalized with respect to their maximum values. The maximum value of both clusters and rest material was used to normalize the rest material to provide an estimate of the relative importance of the nonclustered material amounts. The samples are as follows: C, control with no differential labeling of redox forms and 0, 0.5, 1.7, and 10, which indicate the minutes into the light after dark adaptation (cf. Fig. 1A). Small numbers in the squares indicate the numbers of imputed values replacing missing data, when pertinent. Stars indicate the time points that identify the proteins as displaying a redox effect over time (Hay's post hoc test comparing these time points with tp0 with a *P* value <0.05; no more than 1 imputed value per time point; the significant clusters contain overlapping fractions among all replicates; see Materials and Methods). cpFBPase 1 is not displayed, as its data are too dispersed to pass the selection filters (see data file S3 and Fig. 5B).

TRXf and CDSP32 are directly linked to the photosynthetic electron transfer chain

Electrons transitorily accumulate in the photosynthetic electron transfer chain during induction of photosynthesis. We measured physiological parameters with noninvasive techniques (i.e., CO_2 assimilation and chlorophyll fluorescence) in conditions comparable to those used for our redox proteomic studies (Fig. 2 and fig. S2). While the increase in net CO_2 assimilation occurs mainly within the first 2 min of light (Fig. 3A), photosynthetic electron flux (evaluated as yield of PSII) is transiently quite high and shows a small decrease until ~30 s of light, before increasing and reaching the steady-state level (Fig. 3B). This translates into a Q_A redox state (evaluated with the 1 − qL parameter; Fig. 3C) shifting from fully oxidized to 60% reduced at 30 s and reoxidizing to reach a steady state at ~20% reduced after 7 min of light. The mechanism of photosynthesis induction thus can be divided into three steps. First, between 0 and 30 s, CO_2 assimilation is low (Fig. 3A), showing that the CBC, which is a high-capacity stromal sink for electrons, is not yet operational. As a result, the photosynthetic electron flux decreases while electrons accumulate in the stromal acceptors and then in the photosynthetic

Table 1. Properties of the 27 proteins whose redox states change with time after dark-to-light transfer. The first five columns present data on the tobacco proteins. Prediction of transmembrane domains (TMs) was done with TMHMM; subcellular localization was predicted using TargetP (C, chloroplast; M, mitochondrion; S, secretory pathway; _, other). The last three columns present data for the Arabidopsis homologs of the corresponding POT (Putative Orthologs of Tobacco; see Materials and Methods for a description of the POT system). Whenever possible, the orthologs of the tobacco proteins were selected in the AGI (Arabidopsis Gene Identifier) column, with the exception of cpFBPase 2, absent from Arabidopsis, where the data for cpFBPase 1 are presented. Additional genes of Arabidopsis are as follows: (a) AT4G22890; (b) AT5G16400; (c) AT4G16155; (d) AT5G66570; (e) AT2G41810 and AT3G08030; (f) AT1G78060, AT3G19620, AT5G10560, AT5G49360, and AT5G64570; and (g) AT1G78060, AT3G19620, AT5G10560, AT5G49360, and AT5G64570. Subcellular localization was taken from SUBA4 (pt, plastid; mt, mitochondrion; cyt, cytosol; ec, extracellular). Proteomic studies listed in table S2 were reviewed to find the candidate proteins subject to TRX, CDSP32, NTRC, glutaredoxin (GRX), 2-Cys PRX, and vitamin K epoxide reductase (VKOR) targets (TRX, CDSP32, NTRC, GRX, 2CysPRX, and VKOR, respectively); disulfide bridges (S-S); any oxidation (Sox); glutathionylation (S-SG); nitrosylation (S-NO); sulfenylation (S-OH); and sulfhydration/persulfidation (S-SH).

Tobacco proteins					Arabidopsis homologs			
Protein	**No. of proteins in the group**	**Mean no. of Cys per protein**	**No. of proteins with TM domain**	**Subcellular localization**	**AGI**	**Subcellular localization**	**No. of previous studies**	**Types of previous proteomic studies**
POT000623_2	2	8.5	0	C	AT5G35790	pt	1	S-SH
POT004400	5	5.2	0	C	AT1G32060	pt	12	TRX, GRX, S-S, Sox, S-NO, S-SH
POT007907	2	7	2	M	AT5G22830	pt	0	
POT002945	2	5	0	C	AT4G04640	pt	3	S-S, Sox, S-SH
POT000967b	4	8.8	0	C	AT1G42970	pt	9	S-S, Sox, S-NO, S-SH
POT005070	4	8	0	C	AT3G55800	pt	9	TRX, S-S, Sox, S-NO, S-OH, S-SH
POT007092	2	12	0	C	AT5G13650	pt	4	Sox, S-NO, S-OH, S-SH
POT000179_3	2	6	0	C	AT5G48300	pt	7	GRX, S-S, Sox, S-NO, S-SH
POT007881	3	13	0	C	AT5G14260	pt	3	Sox, S-NO, S-SH
POT010948	2	6.5	0	C	AT1G76080	pt	4	2CysPRX, Sox, S-NO, S-SH
POT003083_1	2	6	2	C	AT4G11960 (a)	pt	1	Sox
POT006052	2	6	0	C	AT3G02730 (b)	pt	4	Sox, S-NO, S-OH, S-SH
POT011766	2	10	0	C	AT5G22620	pt	2	Sox, S-SH
POT005226_3	3	9	0	C	AT5G58330	pt	6	TRX, Sox, S-NO, S-OH, S-SH
POT004591_1	2	10	0	C	AT3G54050	pt	6	GRX, 2CysPRX, S-S, Sox, S-NO, S-SH
POT009251	2	2	2	C	AT1G65230	pt	0	
POT002328_1	2	7	0	C	AT3G16950 (c)	pt	8	TRX, 2CysPRX, S-S, Sox, S-OH, S-SH
POT010360	4	3.5	0	C	AT2G44920	pt	4	TRX, S-S, Sox, S-SH
POT002247	6	4.2	0	C	AT3G50820 (d)	pt	12	TRX, S-S, Sox, S-NO, S-SH
POT010041	2	6.5	0	C/_	AT1G12250	pt	4	TRX, VKOR, Sox, S-SH
POT009086	2	2	0	M	AT3G06050	mt	6	GRX, Sox, S-NO, S-SH
POT001648_1	2	8.5	0	_	AT1G60420	cyt	3	Sox, S-OH, S-SH
POT011141_3	4	8.8	0	S	AT3G56310	ec	3	Sox, S-NO, S-SH
POT001492_2	2	4	0	S	AT2G41800 (e)	ec	2	Sox, S-SH
POT000064_08	3	14	0	S	AT1G02640 (f)	ec	2	Sox, S-SH
POT000215_6	5	7.8	0	S	AT5G67090	ec	0	
POT000064_12	2	18	0	S	AT1G02640 (g)	ec	2	Sox, S-SH

Table 2. Decision table for defining whether the chloroplast proteins are at equilibrium with TRXf. Results of the one-way analysis of variance (ANOVA) comparing the apparent *Em* (*Ea*), calculated at 0.5, 1.7, and 10 min of light from the reduced level of the protein and assuming that it is at equilibrium with TRXf in a two-electron redox reaction. The *P* values were corrected for multiple hypotheses testing with the Bonferroni method, and the maximum threshold for rejecting the equality null hypothesis was set to 0.05. The total number of used *Ea* values is indicated, as well as the average [*Ea* (mV)] and the SD [σ *Ea* (mV)] of *Ea* for the proteins for which no difference between time points was found. The *Em* values found in the literature are also reported (*38*, *39*, *41*, *42*, *44*, *45*). Stars (*) indicate *Em* values that are closer to the average *Ea* than half an SD of *Ea*. na, not available.

Protein	Name	Corrected *P* value	No. of *Ea* values	*Ea* (mV)	σ *Ea* (mV)	Literature *Em* (mV)
POT007092	SVR3	3.90×10^{-7}	24			
POT005070	SBPase	6.60×10^{-6}	24			
POT000967b	GAPB	7.00×10^{-6}	27			
POT009251	CGL52	0.00048	18			
POT000179_3	APS1	0.0014	27			
POT004591_2	cpFBPase 1	0.0041	27			
POT002945	ATPC1	0.01	18			
POT007881	PPKMT1/SAFE1	0.036	27			
POT010948	CDSP32	0.054	27	−282	8	−283* (*41*)
POT005226_3	NADP-MDH ox/half red	0.18	27	−277	9	−283* (*42*)
POT005226_3	NADP-MDH half/fully red	0.27	27	−285	9	−300 to −330 (*42*)
POT011766	CA1Pase	1	21	−264	12	na
POT004400	PRK	1	24	−267	7	−290 (*38*), −295 (*39*)
POT004591_1	cpFBPase 2	1	26	−288	7	na
POT000623_2	G6PD1	1	18	−268	10	−276 (*44*), −318 (*45*)
POT002328_1	PDC-E3	1	27	−282	8	na
POT007907	MGT10	1	24	−268	11	na

chain back to the PSII acceptor Q_A (Fig. 3, B and C). A transthylakoid proton motive force (pmf) builds up, triggering the pH-dependent increase in non-photochemical quenching (NPQ) (Fig. 3B), linked with a transient activation of cyclic electron flow around PSI (*33*). The initial transient high value of the photosynthetic electron flux may be partly due to the use of NADPH to reduce a preexisting pool of 3-phosphoglycerate (3PGA) (*34*). Second, between 30 s and 2 to 3 min, CO_2 fixation and, by inference, the CBC become rapidly activated (Fig. 3A), allowing the photosynthetic electron flux to increase as electrons are partially drained from the photosynthetic chain and Q_A (Fig. 3, B and C). Last, CO_2 assimilation stabilizes between 3 and 10 min (Fig. 3A), and Q_A oxidation does so after 5 min of light (Fig. 3, B and C). By 10 min of light, both CO_2 assimilation and PSII yield have reached the steady-state levels characteristic of plant material at the low light intensity used in this study. The three time points harvested for enzyme redox state measurements thus correspond to (i) the lowest PSII yield at 30 s, (ii) a time just before the end of the fast part of activation of CO_2 assimilation at 1.7 min, and (iii) steady-state photosynthesis at 10 min.

The two chloroplast TRXs TRXf and CDSP32 show a reduction transient at 30 s, coinciding with the temporary overreduction of Q_A and the decrease in photosynthetic flux. TRXf (Fig. 3D) and CDSP32 (Fig. 3E) have both reduced and oxidized clusters that significantly change with time (data file S3 and Fig. 2). TRXf reaches a maximum average of ~40% reduction at 30 s and becomes reoxidized to ~30% reduced form after 10 min of light. For CDSP32, the respective values are ~60% at 30 s and ~30% at 10 min. These changes demonstrate that electrons from the photosynthetic chain are transferred through these redox transporter proteins, thus directly connecting their redox states.

The two other measured chloroplast TRXs, TRXm and NTRC, do not change redox states with time, remaining predominantly oxidized. The results for TRXm (Fig. 3F) are puzzling, since its very low reduced cluster indicates that the protein is always oxidized but hardly any oxidized material is detected. Similar results were obtained for the other two proteins of POT001818, representing other TRXms of tobacco, for which our analysis did not retrieve any clusters (POT001818_1 and POT001818_3; data files S1 and S2). This might be an artifact of the labeling technique in that some PEGylated maleimide (Mal-PEG)–conjugated proteins have been reported to suffer from decreased protein stability (*35*). It is also possible that TRXm has several oxidized forms spread over different fractions of the gel, yielding abundances below the detection threshold in individual fractions. Nonetheless, it appears likely that TRXm remains oxidized during photosynthesis induction in our low-light conditions. NTRC functions as a homomer of subunits bearing one TRX domain and one NTR domain, each with one pair of cysteines (*36*). Therefore, one could have expected to find three distinct redox forms of the subunit corresponding to zero, one, or two reduced cysteine pairs. However, this was not the case (POT009468_2; data file S3), either because both cysteine pairs always have the same redox state, due to having the same midpoint redox potentials (*Em*) (*25*), or because two of the three forms are measured together in our clusters. Overall, our results show that the redox state of NTRC does not change during photosynthesis induction at low light (Fig. 3G) and that the reduced cluster remains at ~20% of the total amount.

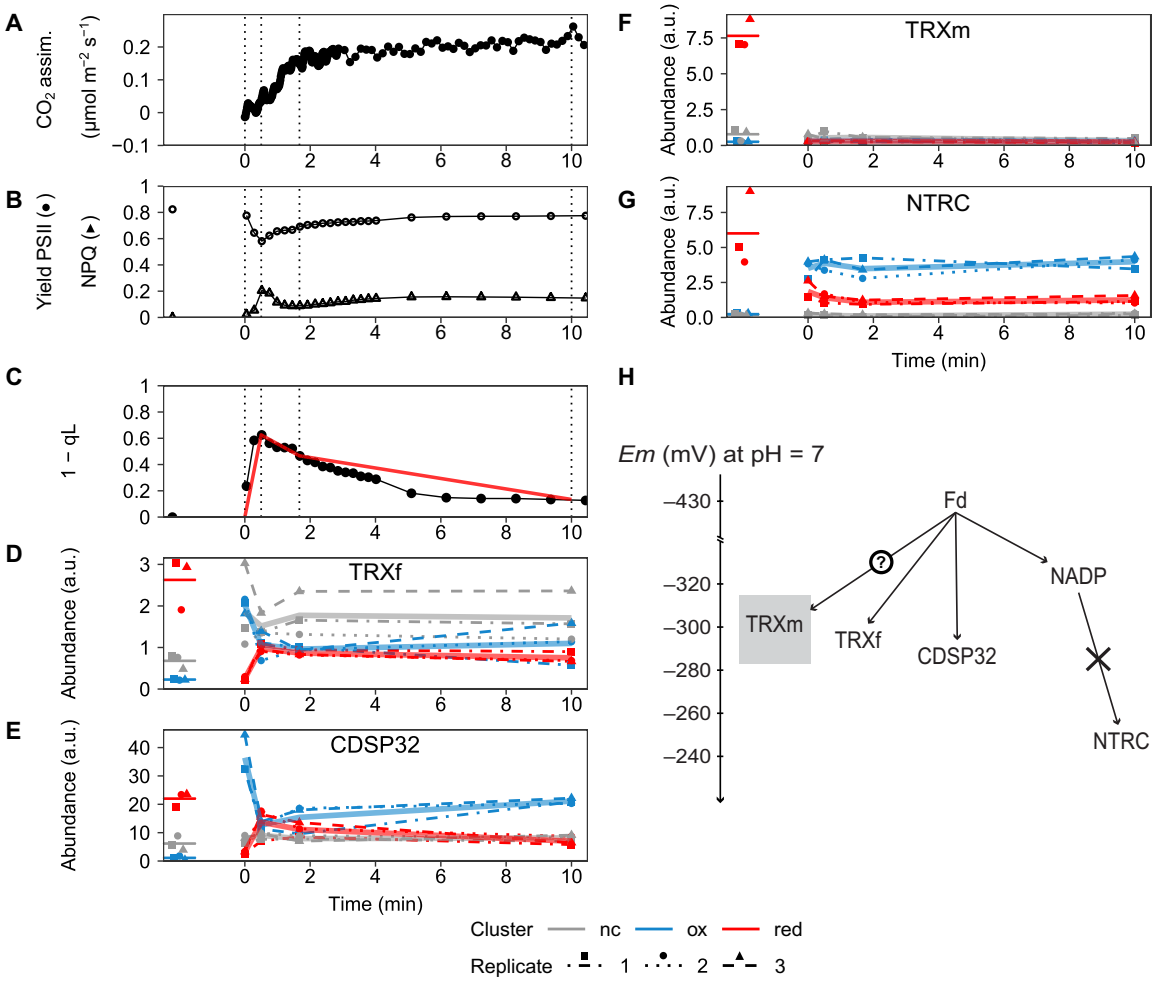

Fig. 3. Induction of photosynthesis analyzed by measurements of chlorophyll fluorescence, CO_2 assimilation, and redox kinetics of chloroplast TRXs. In all experiments, the plant material was placed in darkness for 30 to 45 min before the onset of light at time point 0. (**A**) CO_2 assimilation. Vertical dashed lines show the time points harvested for redox proteomics. (**B**) Yield of PSII and NPQ measured by chlorophyll a fluorescence. The Fv/Fm value was measured 2 min before the onset of light. (**C**) 1 – qL calculated from the chlorophyll fluorescence measurements, representing the redox state of Q_A. The red line displays the same kinetics using only the time points measured with redox proteomics and the Fv/Fm value for time point 0. (**D** to **G**) Kinetics of the reduced (red; red color) and oxidized (ox; blue) clusters and unclustered protein material (nc; gray) for POT006052 (TRXf) (D), POT010948 (CDSP32) (E), POT001818_2 (TRXm) (F), and POT009468_2 (NTRC) (G). The control time point is represented at $t = -2$ min to facilitate visualization, with a horizontal bar for the average of the three replicates. Solid transparent lines depict averages of the three replicates. See Fig. 2 for the significant time points. Please note that, although they are displayed on the same graph, absolute levels of abundance cannot be directly compared between clusters. Instead, the kinetics of the reduced cluster can be directly compared with the control level displayed at $t = -2$ min, which measures the total quantity of the protein in the same gel fraction(s). a.u., arbitrary units. (**H**) Scheme representing the literature values of redox midpoint potentials (*Em*) for the proteins in (D) to (G) (*25*, *37*–*41*).

Regulatory electrons are not distributed evenly between redox transporters downstream of PSI acceptors. If their distribution would be governed by thermodynamics, one would expect the transporters with higher *Em* values to be the more reduced. The scheme in Fig. 3H summarizes the *Em* values found in the literature for the redox carriers measured in our study. Although these *Em* values were not measured for tobacco proteins, several studies performed with different plant species have yielded similar values around −290 mV for TRXf (and different values for the different TRXm isoforms; represented with a gray box in Fig. 3H) (*37*–*40*). The potentially low *Em* of the tobacco POT001818_2 TRXm could explain why this redox carrier remains more oxidized than TRXf during the kinetics. Since the *Em* of CDSP32 was measured as −283 mV in Arabidopsis (*41*), it would be expected that CDSP32 reaches a more reduced state than TRXf in our kinetics. However, if the whole redox regulatory network was at equilibrium, then one also would have expected NTRC [with a much higher *Em* (*25*); Fig. 3H] to be mostly reduced. Thus, kinetic barriers must exist that prevent NTRC, and possibly TRXm, from accepting photosynthetic electrons in our experimental conditions (Fig. 3H). These considerations prompted us to investigate systematically whether the redox-regulated proteins are at equilibrium with TRXf.

Apparent midpoint redox potential calculations clarify whether TRXf and its targets are at equilibrium

We first calculated the kinetics expected for proteins that are in equilibrium with TRXf but have different *Em* values. To this end, we assumed that $Em_{TRXf} = -290$ mV and TRXf is fully oxidized at

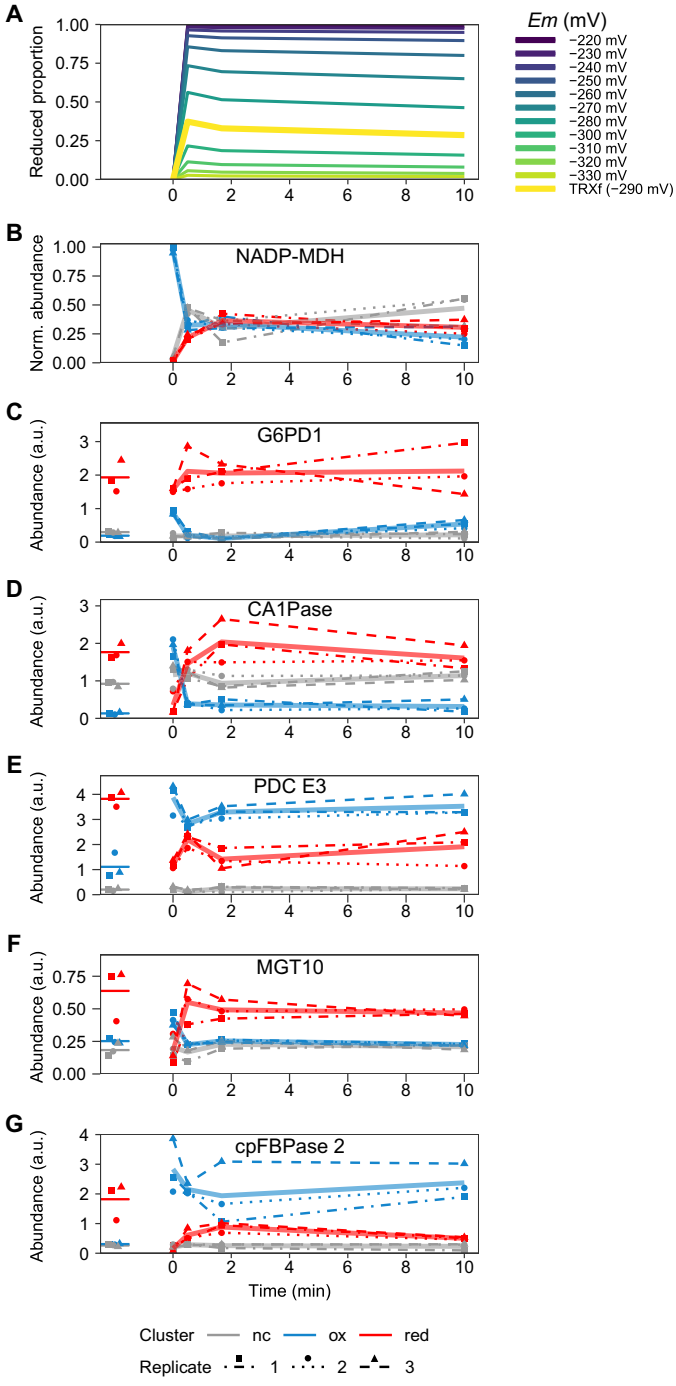

Fig. 4. Modeled and measured redox kinetics of chloroplast proteins at equilibrium with TRXf. (**A**) Expected kinetics for the reduced form of proteins with various *Em* values, if at equilibrium with TRXf. The average of the three replicates of the reduced cluster of TRXf is displayed. (**B**) Kinetics of the proportions of the three redox forms of POT005226_3 (NADP-MDH), measured in fractions 2 (completely oxidized, blue), 3 (half-reduced, gray), and 5 (fully reduced, red), after normalization. (**C** to **G**) Kinetics of the reduced (red) and oxidized (blue) clusters and unclustered material (gray) for POT000623_2 (G6PD1) (C), POT011766 (CA1Pase) (D), POT002328_1 (PDC-E3) (E), POT007907 (MGT10) (F), and POT004591_1 (cpFBPase 2) (G). The control time point is artificially represented at $t = -2$ min, with a horizontal bar for the average of the three replicates. Solid lines depict averages of the three replicates (shown as dashed/dotted lines). See Fig. 2 for the significant time points.

tp0. As seen in Fig. 4A, when the *Em* is very low, the protein remains oxidized, while a high *Em* results in quick and stable reduction. Between these extremes, the kinetics show a transient reduction with different levels of reduction depending on the *Em* of the protein. We then selected chloroplast stromal or thylakoid membrane proteins from our redox proteomic dataset that were classified as showing significant differences over time (Figs. 3, B to G, and 4). These proteins represent potential direct targets of TRXf. We treated the two redox reactions that occur for NADP-MDH separately: (i) the reduction of NADP-MDH–oxidized to NADP-MDH–half-reduced and (ii) the reduction of NADP-MDH–half-reduced to NADP-MDH–fully reduced. Some of the analyzed proteins display kinetics that closely resemble the modeled responses (Fig. 4A), while others deviate substantially.

We then calculated, for each protein and each time point, the apparent *Em* (hereafter named *Ea*) on the basis of the observed reduction level of the protein and assuming that it is at equilibrium with TRXf in a two-electron redox reaction. We tested whether *Ea* values for a given protein differ between time points (Table 2). Proteins that show statistically significant differences (at level $P < 0.05$) are considered to be not at equilibrium with TRXf and will be discussed in the next section. Proteins with no statistically significant difference have no observable change of *Ea* over the kinetics and thus could be at equilibrium with TRXf.

CDSP32 and the N-terminal disulfide bond of NADP-MDH display kinetics compatible with an equilibrium with TRXf during photosynthesis induction. Proteins that show a constant *Ea* during the time series fall into two groups regarding their redox reaction with TRXf. If their measured *Em* is equal to the calculated *Ea*, then our data are compatible with an equilibrium with TRXf. If they are not, then either the literature *Em* (measured in vitro) is different from the *Em* of the tobacco protein in vivo and there could be an equilibrium corresponding to the calculated *Ea*, or there is a kinetic constraint on the redox reaction and this has a constant effect on the *Em*-*Ea* difference. To distinguish between these two scenarios, available literature *Em* values were compared with the *Ea* values. They were accepted as equal when their difference did not exceed half an SD of the calculated *Ea* (Table 2). This is the case for CDSP32, as was already apparent from the shapes of the kinetics and Fig. 3E. For NADP-MDH, the *Ea* value is consistent with the *Em* value of the N-terminal disulfide bond measured for the sorghum enzyme, which corresponds to the reduction of the fully oxidized to the half-reduced enzyme (*42*). However, we find that the *Ea* for the second reduction of the enzyme is more positive than the measured values in the same study (Table 2). This discrepancy could be due to the different species or to differences related to C_3 versus C_4 metabolism or reflect some in vivo kinetic constraint influencing the *Ea*, which thus approaches the Em_{TRXf} level. Our method does not allow us to identify which cysteines are reduced or oxidized in each of the three measured forms, which would be crucial to completely understand the enzyme activation and assess the possible role of allostery in it (*43*). The two-step activation of NADP-MDH allows the fully reduced form of the enzyme to appear with a delay compared to the reduction peak experienced by TRXf and the photosynthetic chain in the first 30 s of light. This could ensure that the photosynthetic electrons transferred to NADPH are used to build up the pools of CBC intermediates during the fast activation phase, instead of them being exported out of the chloroplast by the malate/oxaloacetate shuttle in which NADP-MDH is involved. The fully reduced form then decreases in parallel to TRXf. If the light intensity would rise after this first activation, one can hypothesize that the fully reduced form of NADP-MDH would not show such a delay since the partially reduced form (~50% of the total amount at 10 min; Fig. 4B) remains available for further reduction.

PRK and G6PD1 have much higher *Ea* values than the *Em* values reported in the literature, making it difficult to draw firm conclusions. For both enzymes, the *Ea* value is above Em_{TRXf}, while the measured *Em* is lower than Em_{TRXf} (Table 2). Since their redox states are almost fully reduced for the three time points used to calculate the *Ea* values, they would be found having constantly high *Ea* values in redox reactions with all possible kinetics not only the specific one of TRXf (Fig. 4A). Note that there are two different values for G6PD1 in the literature, of which one is quite close to our *Ea* value (Table 2) (*44*, *45*). G6PD1 is also partially reduced at tp0, when TRXf is probably completely oxidized (Fig. 4C), which fits with the *Ea* of G6PD1 being higher than the *Em* of TRXf. This high *Ea* value allows the enzyme to be quickly inhibited at the onset of light, allowing the CBC to become activated without interference of the OPPP. G6PD1 becomes slightly reoxidized at steady-state light (Fig. 4C, blue curve), lending support to the hypothesis that the glucose-6-phosphate shunt of the CBC reactions regenerating ribulose-5-phosphate from fructose-6-phosphate can function in the light (Fig. 5J) (*45*). The *Ea* value of PRK is also above Em_{TRXf} and Em_{PRK} (Table 2), with its kinetics showing a fast and total reduction (Fig. 5A). An explanation could be the reported increase in the *Em* of PRK in the presence of Mg^{2+} and the PRK substrate ATP (*46*), both of which increase levels in the light.

For the four other identified proteins (i.e., CA1Pase, MGT10, PDC-E3, and cpFBPase 2) whose *Ea* values do not change over time, there are no reports of *Em* values in the literature. Therefore, we cannot test whether they are at equilibrium with TRXf. CA1Pase (POT011766), a regulator of Rubisco, has been shown to be redox-regulated in tobacco (*47*). Its fast reduction to almost 100% would be consistent with its function in photosynthesis induction, but the obtained reduction curve probably does not fully reflect the activity of the protein, which is also regulated by fructose-1,6-bisphosphate (FBP). The dihydrolipoamide dehydrogenase (PDC-E3, POT002328_1) is part of the pyruvate decarboxylase complex in the chloroplast. Its active site uses redox chemistry of cysteines to transfer electrons from dihydrolipoamide to NAD^+ (*30*). The recorded kinetics are thus not the result of a redox regulation but rather reflects the change in accumulation of the four-electron reduced dead-end state (also called S4) (*48*), an inhibited form of the enzyme. The S4 proportion is determined by the redox state of NAD [nicotinamide adenine dinucleotide (oxidized form)], the stromal pH, and the lipoamide/dihydrolipoamide product/substrate ratio (*48*). During photosynthesis induction, with the increasing stromal pH from 7 to 8, the observed increase in S4 between 0 and 30 s of light should be accompanied by a decrease in the NAD^+/NADH ratio, according to the model (*48*). Since the NAD^+/NADH and $NADP^+$/NADPH ratios in the chloroplast are linked by several enzymatic reactions, a decrease in the NAD^+/NADH ratio can result from an increasingly reduced NADP pool in the initial stage of photosynthesis induction. The decrease in S4 observed after 30 s of light is less straightforward to explain: According to the model, it could be due to an increase in the NAD^+/NADH ratio, which could be the result of a reoxidizing NADP pool, or an increase in the lipoamide/dihydrolipoamide ratio. The two remaining proteins, the Mg^{2+} transporter MGT10 and a

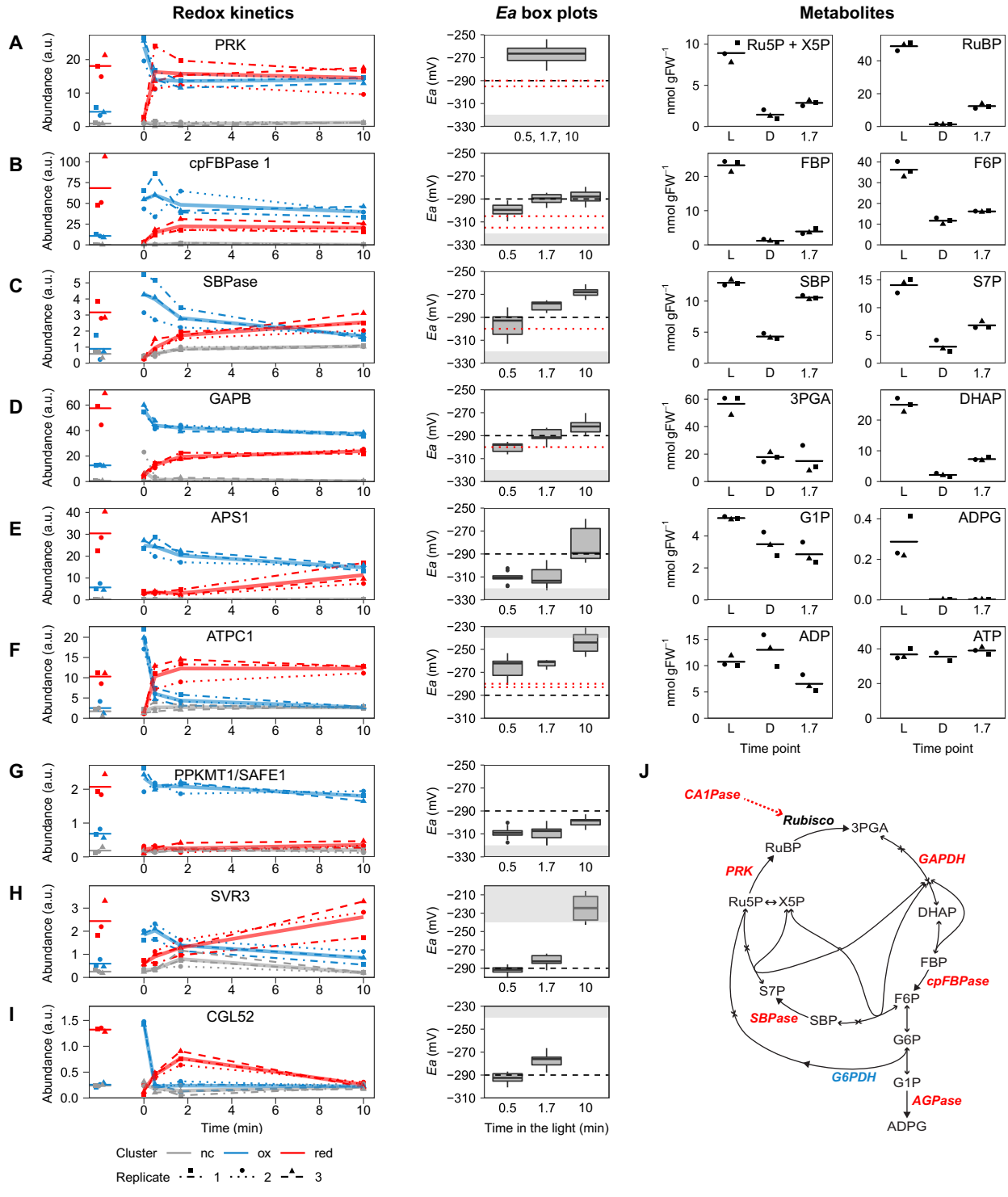

Fig. 5. Analysis of the proteins with varying *Ea* values over time and PRK. Redox kinetics: Redox proteomic kinetics for reduced (red) and oxidized (blue) clusters and unclustered material (gray). Imputed values not based on two measurements are around 0.2 (CGL52, 10 min). Corresponding sPOTs: (**A**) POT004400, (**B**) POT004591_2, (**C**) POT005070, (**D**) POT000967b, (**E**) POT000179_3, (**F**) POT002945, (**G**) POT007881, (**H**) POT007092, and (**I**) POT009251. *Ea* box plots: Distributions over time of the apparent *Em* (*Ea*), calculated from the reduced level of the protein, assuming it is at equilibrium with TRXf in a two-electron redox reaction. Box width is proportional to its number of values. Dashed black lines represent the Em_{TRXf} level, and dotted red lines represent the available *Em* values in the literature (*38*, *39*, *110*, *111*). Gray areas show *Ea* ranges where the calculations cannot give precise results (see Fig. 4A). Metabolites: Upstream (left) and downstream (right) metabolites for measured enzymes and scheme showing the enzymes in the redox color of their active form (**J**). All metabolites were measured in the same nine samples, corresponding to three time points: steady-state growth light (L) at 9 hours of daylight, 30 to 45 min of darkness after time point L (D), and 1.7 min of growth light after time point D (1.7). Crossbars represent the averages of three measurements (triangle, circle, and square). Measured contents are total cell contents, and fractions present in the chloroplast can be found in (*103*).

second chloroplast fructose-1,6-bisphosphatase (cpFBPase 2), will be discussed in the following paragraphs.

Most redox-regulated carbon metabolism enzymes show reduction curves controlled by kinetic constraints

Among the proteins whose *Ea* values change with time (Fig. 5), four are crucial for chloroplast carbon metabolism: cpFBPase 1 (Fig. 5B), SBPase (Fig. 5C), GAPB (Fig. 5D), and APS1 (Fig. 5E). The *Ea* values at 0.5 min of light are close to the *Em* values measured in vitro [red dotted lines; see box plots in Fig. 5 (B to D)]. For cpFBPase 1, SBPase, and GAPB, these *Em* values are lower than the Em_{TRXf} (black dashed lines). The *Ea* values then increase to reach Em_{TRXf}, for cpFBPase 1, or exceed it, for SBPase and GAPB. This effect indicates that kinetic constraints first hinder and then favor the reduction of these proteins by TRXf. Kinetic constraints could originate from intrinsic properties of the targets that make the reduction reaction very slow, as suggested for SBPase based on in vitro studies (*19*). The kinetic constraints could also result from changes in regulatory metabolites that affect the rate of reduction and/or the mid redox potential of the cysteine pair on the target protein. The apparent *Em* of cpFBPase 1 has been shown to increase in the presence of its substrate FBP (*46*). It is plausible that an analogous mechanism exists for SBPase [see (*10*)].

Next, we measured the contents of FBP and other metabolites related to the CBC (Fig. 5, column "Metabolites"). The FBP content slightly increases between darkness (D) and 1.7 min of light (1.7), which could account for the *Ea* increase of cpFBPase up to Em_{TRXf} at 1.7 min of light. The following large increase of FBP amount between 1.7 min and L (steady-state light) does not translate into an increase of the reduced proportion of cpFBPase 1, leaving the enzyme at an *Ea* level comparable to the *Ea* at 1.7 min and similar to Em_{TRXf}. Regulation of the *Em* by metabolites has not been demonstrated for the other enzymes in Fig. 5, but their activities are known to be regulated by various metabolites (*9*, *10*, *49*). These could directly affect enzyme activities or indirectly affect the regulation of the redox states, as proposed previously (*9*). In our samples, most CBC metabolites, including substrates, products, and regulators of the CBC enzymes, show an increase in concentration as photosynthesis is activated. 3PGA, glucose-1-phosphate (G1P), and ADP-glucose (ADPG) are exceptions, in that their concentrations remain stable between the D and 1.7 min time points and rise only at steady state (Fig. 5, column "Metabolites"). The increase in G1P and ADPG at a late stage of photosynthesis induction is in agreement with the export of CBC products starting after a phase of intermediate pool building and fits with the delayed redox activation of ADP-glucose pyrophosphorylase (AGPase) (Fig. 5E). Regulation of the *Em* of APS1 may occur by its substrate or by the 3PGA/Pi ratio that increases after 1.7 min of light [due to the rise in 3PGA and the decrease in Pi linked with the increase in all CBC metabolites; see (*50*)]. ADP decreases between darkness and 1.7 min of light, whereas the level in steady-state light is comparable to that in darkness. ATP thus accumulates in the stroma at 1.7 min, even if this is not visible from the total cellular ATP levels (*51*). The rise in chloroplast ATP is consistent with the ATP synthase being active at this time point and is also in agreement with the low NPQ measured and the CBC not yet operating at steady state. Accordingly, the gamma subunit of ATP synthase becomes reduced quickly and fully (Fig. 5F), as already shown with functional measurements (*52*) and immunoblot analyses (*53*). Its *Ea* is always above the measured *Em* values, indicating activity of a mechanism that reduces ATPC1 and maintains it in a reduced state while TRXf becomes reoxidized.

The multiple levels of regulation of CBC enzyme activities raise the question of whether the in vivo activities reflect only their redox states or whether these activities are at least partly determined by other regulatory factors. To address this point, we assumed that no other factors regulate these enzymes and calculated the required redox changes between 1.7 min and steady-state light on the basis of the measured changes in CO_2 assimilation and metabolite levels for the three redox-regulated irreversible enzymes of the CBC (PRK, cpFBPase, and SBPase). CO_2 assimilation was used as a proxy for the flux rate through the CBC and the three enzymes. For each enzyme, this rate was corrected for nonsaturating substrate concentrations using the calculated stromal substrate concentrations based on our metabolite measurements and K_M values retrieved from the literature (see Materials and Methods; Eq. 7). At 1.7 min of light, CO_2 assimilation is at ~75% of its steady-state value (Fig. 3A and fig. S2). According to Eq. 8, the reduced forms of the enzymes at 1.7 min should be at 90% for SBPase ($\sigma = 8\%$), 370% for cpFBPase ($\sigma = 70\%$), and 250% for PRK ($\sigma = 60\%$) of their steady-state values. Thus, while SBPase is predicted to become slightly reduced in this late phase of photosynthesis induction, cpFBPase and PRK are predicted to become substantially oxidized. We calculated the same ratios based on our redox proteomic datasets and obtained 70% for SBPase ($\sigma = 10\%$; Fig. 5, kinetics C), 110% for cpFBPase 1 ($\sigma = 20\%$; Fig. 5, kinetics B), 170% for cpFBPase 2 ($\sigma = 20\%$; Fig. 4G), and 110% for PRK ($\sigma = 20\%$; Fig. 5, kinetics A). Both calculations provide qualitative matches for SBPase and cpFBPase 2, while the observed redox changes of cpFBPase 1 and PRK cannot be inferred from the relation between substrate levels and flux. PRK shows almost maximal reduction at 1.7 and 10 min (redox proteomics), but its activity is probably not maximal at either time points. At 1.7 min, the CBC is partially active and the enzyme is probably substrate-limited. At 10 min, the predicted more oxidized PRK could result from the inhibition by 3PGA, FBP, and/or RuBP (ribulose-1,5-bisphosphate), metabolites that all increase greatly between 1.7 min and steady-state light (Fig. 5, column "Metabolites") and are known inhibitors of the reduced form of the enzyme (*10*, *54*).

New redox-regulated proteins provide fresh insight into chloroplast physiology and evolution of redox regulation

A second cpFBPase, cpFBPase 2, shows a different redox kinetics from the previously most-studied cpFBPase (cpFBPase 1), as well as differs in the sequence of its redox-sensitive insertion and active site (Fig. 6A). cpFBPase 2 shows reoxidation after 1.7 min, while the redox state of cpFBPase 1 remains stable (Figs. 3G and 4B). The amino acids surrounding the three cysteines in the redox-sensitive insertion differ between both cpFBPases, particularly in the arrangement and number of charged amino acids (Fig. 6A). It has been proposed that the regulatory TRX recognizes this exposed region by electrostatic interactions (*55*), possibly suggesting that the observed differences in reduction kinetics originate from these sequence differences. Furthermore, three amino acids participating in the active site of the enzyme differ in cpFBPase 2 compared to cpFBPase 1 and cytosolic FBPase. Notably, Tyr^{347}, binding the 6-phosphate of FBP, and Lys^{357}, binding the fructose of FBP (*56*), are both replaced by asparagines in cpFBPase 2 (Fig. 6A). These changes make the entrance of the active site larger in the structural model of cpFBPase 2 than in those of cpFBPase 1 and cytFBPase and in the crystal structure of pea cpFBPase 1 (Fig. 6, B to E). The cpFBPase 2 is not present in *Arabidopsis thaliana*, which probably results from a secondary loss

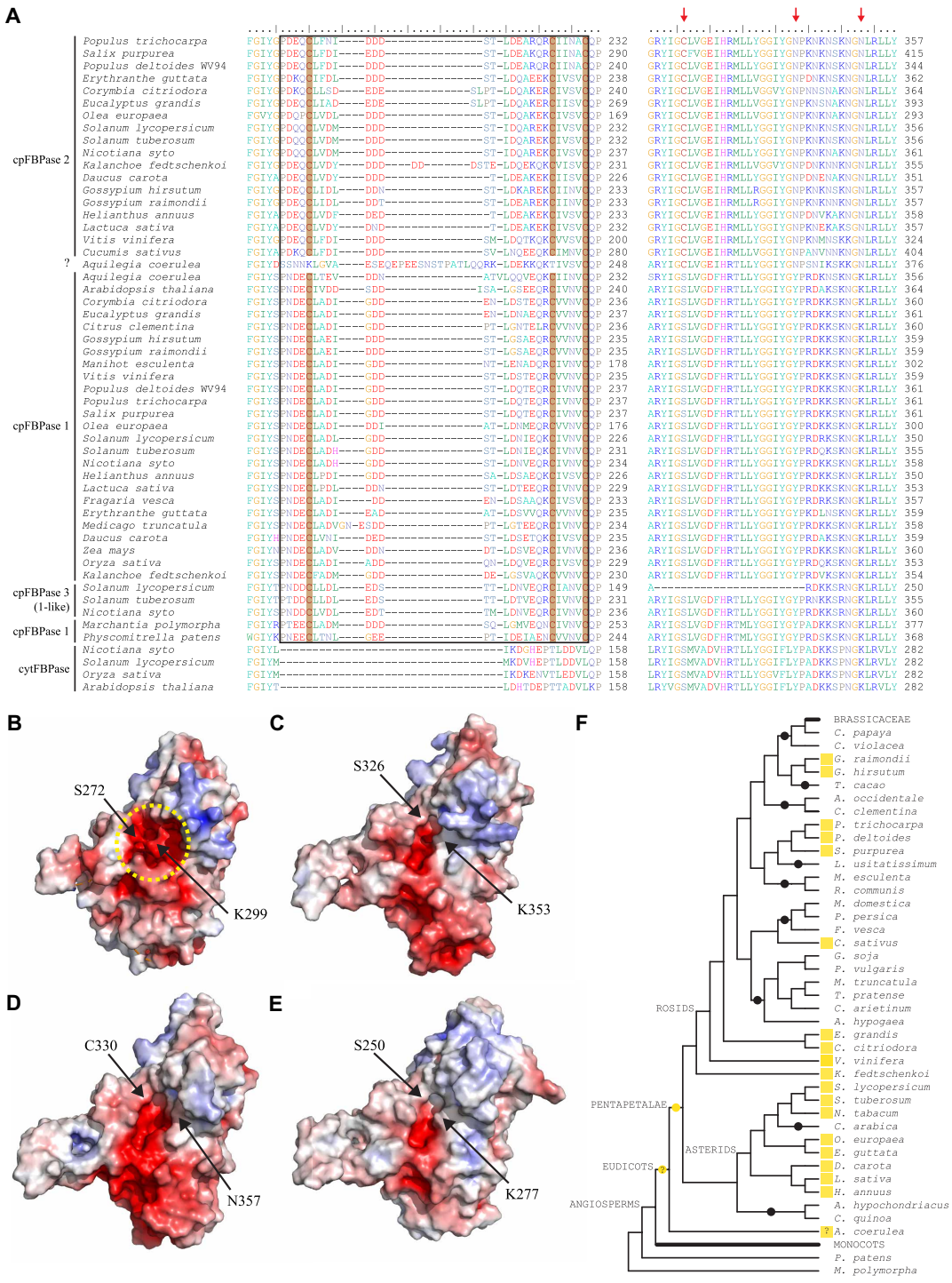

Fig. 6. Sequence analysis and structure of tobacco cpFBPase 2. (**A**) Amino acid sequence alignment of two regions of cpFBPases 1, 2, and 3, including all available cpFBPase 2 and 3, selected cpFBPase 1, and four cytosolic FBPase sequences. *Nicotiana syto* stands for the pooled sequences of *Nicotiana sylvestris* and *Nicotiana tomentosiformis* used in this work, of which only one gene per protein group is displayed. Similarly, only the A genome version of *Gossypium hirsutum* is displayed because the D genome version is identical to the *Gossypium raimondii* sequences for both regions. Physicochemical properties are color-coded. The redox-sensitive insertions of cpFBPases (black frame) contain three redox-active cysteines highlighted in brown. Red arrows mark three active site substitutions between cpFBPases 1 and 2. (**B** to **E**) Electrostatic surface (red, negative; blue, positive) views showing the entrance of the active site (dashed yellow) of the crystallized oxidized pea cpFBPase (Protein Data Bank 1D9Q) (B) and I-TASSER models for the tobacco proteins POT004591_2 (cpFBPase 1) (C), POT004591_1 (cpFBPase 2) (D), and POT000761_1 (cytFBPase) (E). The two facing amino acid substitutions in the active sites of cpFBPases 1 and 2 are indicated. (**F**) Cladogram of corresponding species showing the presence of cpFBPase 2 (yellow squares). Yellow and black circles indicate gain and loss events of cpFBPase 2, respectively. *Aquilegia coerulea* has a sequence with the active site of cpFBPase 2 and a divergent one-cysteine redox-sensitive insertion. Protein IDs and full names of species are in table S3.

during evolution (Fig. 6F). By contrast, the genome of *Cucumis sativus* seems to be devoid of a cpFBPase 1, indicating that cpFBPase 2 probably has fructose-1,6-bisphosphatase activity. The tomato and potato homologs of cpFBPases 1 and 2 are the most highly expressed isoforms in the chloroplasts of leaves, in contrast to cpFBPase 3 (POT004591_3 in tobacco, not detected in our study) that is expressed to much lower levels (*57*). High FBP content is a specific feature of the CBC metabolite signature in tobacco, while eight other tested species have low FBP/F6P ratios (*58*). The latter group lacks cpFBPase 2, with the exception of two C4 *Flaveria* species whose publicly available RNA sequencing data (*Flaveria bidentis*, SRR1165185; *Flaveria trinervia*, SRR1166378) were found to contain cpFBPase 2 sequences. In summary, cpFBPase 2 is an enzyme with a potential role in fine-tuning of photosynthetic metabolism, whose substrate specificity and kinetic parameters warrant further investigation.

The plastidial magnesium transporter MGT10 (also described as MRS2-11; POT007907) is a strong candidate for a new TRXf target, as evidenced by its rapid and complete reduction in the light (Fig. 4F). MGT10 belongs to the well-characterized CorA-MRS2-ALR magnesium transporter superfamily found in all living organisms. The tobacco proteins have the conserved Gly-Met-Asn motif characteristic of functional Mg^{2+} transporters (fig. S3). Compared to its bacterial homolog CorA, the plant MGT10 has an insertion that is rich in acidic amino acids and contains four to five conserved cysteines (fig. S3A). Compared to the structure of the crystallized CorA transporter, the insertion is located at the exit channel of the transporter (fig. S3, B to D). Cysteines C1, C2, and C3 are located in an accessible loop in the structural model and thus are probable candidates for redox regulation (fig. S3D). In addition, the surface of the region containing these cysteines is electronegative (fig. S3E), making it a potential interaction surface for TRXf. The Arabidopsis homolog AtMRS2-11 is located in the chloroplast and mostly present in the envelope (*59*), suggesting that the in silico prediction of mitochondrial targeting for POT007907 is likely incorrect (Table 1). It, therefore, seems reasonable to speculate that redox regulation modulates the activity of the transporter, thus controlling the magnesium concentration in the stroma and even the cytosol in a light-dependent manner.

Three proteins whose redox states are controlled by kinetic constraints were not previously known to be redox-regulated: PPKMT1/SAFE1 (POT007881), which becomes reduced late in photosynthesis induction, CGL52 (POT009251), and SVR3 (POT007092), whose reduction stretches over the whole process of photosynthesis induction (Fig. 5, G to I, and data file S3). CGL52 (conserved in the green lineage 52) is a ~26-kDa protein that is predicted to harbor a single transmembrane helix at its C terminus. It has only two cysteines, at the N-terminal end of its globular domain, both surrounded by acidic residues (fig. S4A). No function is known for this protein yet. PPKMT1/SAFE1 is a SET-domain potential methyltransferase with unknown substrate specificity. It was shown to be involved in the protection of grana margin proteins upon $^1O_2$ stress (*60*). PPKMT1/SAFE1 protein was found to interact with three plastid-localized proteins in *A. thaliana:* OBERON1 (a protein with a homeodomain finger, a domain that can read methylation patterns), TRXm1, and HEMA1 (glutamyl-tRNA reductase, the enzyme catalyzing the first committed step of tetrapyrrole biosynthesis) (*61*), interactions that seem consistent with the function of a $^1O_2$-linked redox-regulated methyltransferase. One of its seven cysteines is part of a degenerated TRX active site motif, WCGPQ (instead of WCGPC; red frame in fig. S4B), that is located in the predicted SET domain and not found in other SET proteins. SVR3 is a putative translation elongation factor of the BipA/TypA superfamily, whose Arabidopsis homolog has been suggested to play a role in D1 protein accumulation (*62*). SVR3 could be part of a (hypothetical) protein complex that conducts the PSII repair cycle and is subject to redox regulation. Two of the six cysteines in SVR3 are embedded in an ICAIC motif that is similar to the NTR-domain active site ACAIC of NTRC and thus could be potential target residues of redox regulation (fig. S4C).

Last, our data also draw attention to a recent evolutionary loss of redox regulation of Rubisco activase. The tobacco protein encoded by the long splice variant lacks the two cysteines in the C-terminal domain that confer redox regulation in all other plant species expressing a similarly long protein variant (*63*). Accordingly, no oxidized cysteines were measured for Rubisco activase in our experiment (POT001437; data files S1 and S2).

DISCUSSION

A new method for simultaneous recording of redox kinetics

This study presents a novel approach using a combination of time-resolved MS and evaluation algorithm to associate redox proteomics with physiology. Our sampling is based on rapid quenching of leaf juice (*12*) from easy-to-squeeze tobacco leaves, which gives access to membrane (MGT10 and CGL52) and soluble redox-regulated proteins. This harvesting procedure is fast enough to study stable redox modifications of cysteines such as disulfide bonds, as shown in studies using similar protocols in combination with enzyme assays (*10*, *12*), which yielded similar dynamics of the in vitro activities of several CBC enzymes. It might be limited at the very beginning of the kinetics, when fast redox changes could take place. We then differentially labeled the cysteines according to their redox states (*64*), increasing the molecular weight of the oxidized forms. Following in-gel separation, this approach allows the quantification of the reduced form of enzymes, because it can be measured in the same gel fraction(s) as the total amount of the protein in the unlabeled control sample (Fig. 1). We quantified the proteins using all peptides except the cysteine-containing ones, by mapping them to an optimized proteome database for tobacco. Our analysis based on the negative longitudinal relationship of the oxidized and reduced forms provides an automated processing of the gel profile for each protein. Our method is very well suited for proteins with one or two regulated cysteines but may produce less conclusive results for proteins with multiple cysteine residues that are separately regulated and thus are present in more than two redox forms. Although regulated cysteines cannot be identified directly, various time effects of redox regulation are accessed using between-replicate dispersion estimates. Our study provides a temporally resolved proteomic analysis of redox regulation during photosynthesis induction. It can readily be refined in the future by increasing protein coverage or improving early time point measurement and time resolution, and can be used to explore other physiological transitions.

Stromal network of redox regulation

Our results throw light on the topology of the stromal electron transport network in vivo. Similar to its thylakoid counterpart, the photosynthetic electron transport chain, it consists of a network of redox reactions, some of which are presumably at equilibrium while others are clearly controlled by kinetic constraints (Fig. 7). Of

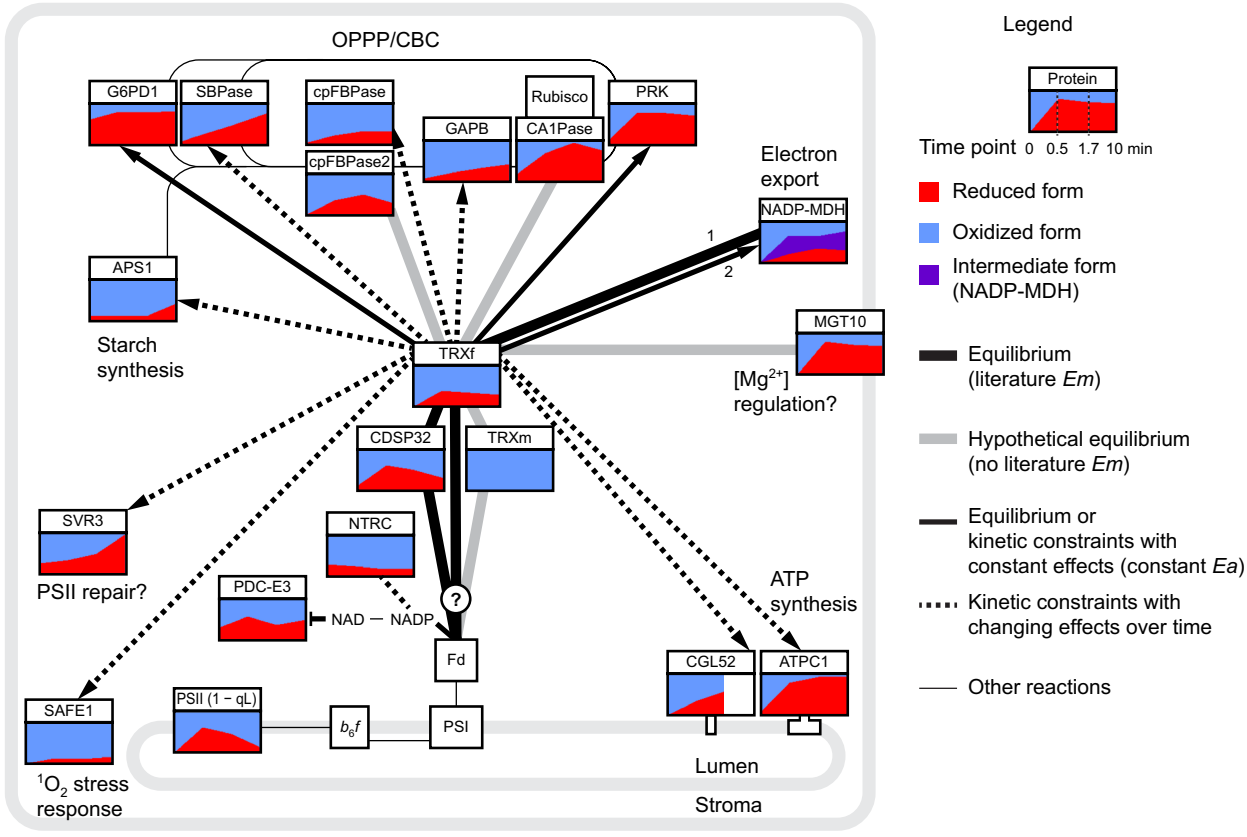

Fig. 7. Schematic view of the chloroplast network of redox-regulated proteins. The reduced and oxidized forms of redox-regulated proteins are depicted in red and blue, respectively. Their relative proportions displayed in the graphs were calculated from the average of the measured reduced kinetics (or, for NADP-MDH, as described in Materials and Methods). Proteins are connected with lines indicating the nature of the redox reaction. TRXf and CDPS32, at equilibrium, are connected by a thick black line. As they may exchange electrons through ferredoxin (Fd), Fd is also linked to them with thick black lines. All other proteins (except PDC-E3) are depicted with their reactions with TRXf, as determined in this study. Corresponding reactions are represented by thick black (equilibrium not excluded), thick gray (kinetic constraints either absent or constant over time, but this cannot be evaluated because of lack of *Em* data in the literature), thin black (kinetic constraints with a constant effect along time), or thin dotted lines (kinetic constraints with changing effects over time). Arrows represent the kinetic constraint effect (solid lines) or change over time (dotted lines) on electron transfer reactions. The reduction reactions of NADP-MDH are indicated with 1 (oxidized to intermediate form) and 2 (intermediate to reduced form). The PSII Q_A redox kinetic is reproduced from Fig. 3C.

the four chloroplast TRXs measured, only TRXf and CDSP32 react in parallel to rapid changes in photosynthetic electron flux (Fig. 3, D and E). TRXf was shown by mutant analyses to be involved in photosynthesis induction (*17*, *18*) and in reduction of CBC and other enzymes (*40*). Its target interactome has not been directly investigated, but its mode of interaction with targets by electrostatic complementarity is well described (*55*). In addition, partially correlated changes in the redox state of TRXf and the photosynthetic flux were observed at different steady-state light intensities (*21*). CDSP32 is a large TRX of 32 kDa responsible for electron transfer to the reactive oxygen species–detoxifying 2-Cys PRXs and 1-Cys methionine sulfoxide reductase (*41*, *65*). Its redox responsiveness to photosynthesis induction suggests that CDSP32 may alleviate oxidative stress during this transition.

Different mechanisms could establish an equilibrium between TRXf and CDSP32. First, TRXf and CDSP32 could directly exchange electrons. Although not yet described for these two proteins, redox exchanges have been shown between TRXs and NTRC (*25*, *66*). Second, TRXf and CDSP32 could be at equilibrium with a third partner, be it ferredoxin via ferredoxin:thioredoxin reductase or an unknown shared partner. If TRXf and CDSP32 are linked via ferredoxin, it needs to be explained why both TRXs remain partially oxidized (Fig. 3, D and E) when linear electron transfer is limited by the CBC (Fig. 3, A to C). A transient activation of cyclic electron flow could decrease linear electron flow by activating NPQ (Fig. 3B) or through photosynthetic control. The transfer of electrons from PSI to oxygen would also divert electrons away from stromal photosynthetic reactions. Both mechanisms would allow ferredoxin to remain partially oxidized. Alternatively, reduction of TRXf and CDSP32 by the same FTR could be kinetically limited. No data are available on the catalytic rate of FTR. However, there may be kinetic limitations due to low abundance or slow diffusion of ferredoxin and/or FTR or due to compartmentation of the pools of TRXf, CDSP32, or ferredoxin. Our results, obtained at low light intensity, differ from a high-light photosynthesis induction experiment performed with *A. thaliana* in (*19*). High light intensity will saturate the redox system with electrons, making it possible to clarify the kinetic limitation of reduction of some targets but not to explore the potential equilibria between TRXs and their targets or the relationship between the electron transfer chain and the stromal redox network.

The redox states of TRXm and NTRC do not follow that of the photosynthetic electron transfer chain. TRXm probably remains oxidized during the whole induction kinetic (Fig. 3G). This would reflect an equilibrium with ferredoxin only if Em_{TRXm} is very negative (Fig. 4A), which is possible (*37*). TRXf and TRXm have overlapping target sets but interact with them at different efficiencies (*14*, *40*). A system with low (TRXm) and high (TRXf and CDSP32) redox potential TRXs could allow for some flexibility in the regulatory network, for example, by reduction of TRXf but not TRXm in low light. Furthermore, TRXm would reduce its targets as a priority during photosynthesis induction, while the reduction of targets by TRXf would depend on redox proportions and other constraints applying to the reactions. In contrast to TRXm, NTRC would be expected to be more reduced than TRXf if all reactions in between would be at equilibrium since its reported *Em* is −245 mV in *A. thaliana* (*25*). This is not the case in our datasets, except in the dark (Fig. 3H). NTRC can indeed be reduced by NADPH from the OPPP in the dark. In the light, electrons must flow from ferredoxin to NADP with a simultaneous increase in CO_2 assimilation (Fig. 3), and the correlation between the redox states of PSII, PSI, and NADP is well documented (*67*). We thus conclude that the reaction between NADP and NTRC is out of equilibrium in our conditions (Fig. 7), and NTRC is not linked to photosynthetic electrons. This finding provides an interesting perspective on the function of NTRC in the reduction of 2-Cys PRX. The current model for the oxidation of redox-regulated enzymes involves a system with H_2O_2, 2-Cys PRXs, and electrons provided by NTRC (*22*–*24*, *68*). A scenario in which NTRC is oxidized and isolated from the photosynthetic electron pathway would allow the redox targets to be selectively activated during photosynthesis induction, while H_2O_2-detoxifying electrons could be provided by CDSP32. Once photosynthesis is activated, a redox balance would be established to accommodate changes in light intensity, with electrons originating from NTRC, CDSP32, or the partially reactivated G6PDH (Figs. 3 and 5C).

Activation of chloroplast metabolism

Overall, our analyses give access to the mechanism mediating activation of chloroplast metabolism by light (Figs. 4 and 6). After 30 s of light, the CBC enzymes are still mostly oxidized, which is probably due to low levels of their regulatory metabolites, with the exception of the fully reduced PRK. ATP synthase is almost completely reduced and can synthesize ATP using the high pmf that has been built up. As the CBC is operating only slowly, accumulation of the first products of the electron transport chain (ATP and NADPH), together with inactive secondary reactions, leads to the buildup of electrons in the photosynthetic chain and in connected redox regulators (TRXf and CDSP32). After 1.7 min of light, cpFBPase 1 and GAPDH have reached their redox steady states, while SBPase is still only 70% reduced. Because of its rapid redox activation, PRK has the capacity to catalyze rapid flux already early in the kinetics. This explains the large increase in CO_2 assimilation and the incipient reoxidation of the photosynthetic chain and redox regulators between 30 s and 1.7 min. The final increase in CO_2 assimilation corresponds to the remaining redox activation of SBPase and to a general increase in CBC metabolite pools that will promote flux through many of the CBC enzymes. This will also be aided by the increase in stromal pH and Mg^{2+} concentration (*69*–*71*). The result is an increase in CBC flux, leading to the increasingly rapid production of 3PGA. NADPH and ATP are thus consumed at a higher rate, allowing the photosynthetic chain and the stromal redox network at equilibrium (redox transporters, NADP-MDH, cpFBPase 2, and PDC-E3) to partly be reoxidized. Concomitantly, CBC products start to be exported with the activation of AGPase and starch synthesis as well as sucrose synthesis (*72*), although the latter was not investigated here.

Changes in the redox states of SBPase and cpFBPase 2 can be qualitatively predicted from changes in their required reaction rates (in combination with their kinetic properties and measured substrate levels) in the second part of photosynthesis induction, showing that the redox state of these two enzymes is a major determinant for their activity. For PRK on the contrary, the putative oxidation predicted from reaction rates is not found in redox proteomic data. Deactivation of cpFBPase, but not of PRK, was already reported for the second stage of photosynthesis induction in maize (*73*). One should keep in mind that in vitro activity measurements reflect redox changes of enzymes when performed in conditions that are optimal to reveal the corresponding changes in kinetic parameters: close-to-reduced-K_M substrate concentrations for redox modifications of the K_M (cpFBPase and SBPase) and high substrate concentrations for modifications of the *kcat* (PRK) (*10*). Accordingly, our redox proteomic kinetics are coherent with previous studies measuring enzyme activity kinetics in different plant species (*10*, *12*, *19*, *67*, *73*).

To uncover cases where the relationship between the redox state of TRXf and its target proteins changes during induction, we calculated *Ea* (i.e., the predicted mid redox potential of the target based on its reported *Em* and assuming it to be in equilibrium with TRXf). Changes in *Ea* during induction imply either that there is a kinetic limitation on the reduction of the target or that kinetic constraints alter the in vivo mid redox potential, leading to it differing from *Em*, as measured in vitro under standard conditions. All enzymes with changing *Ea* values show an *Ea* increase during photosynthesis induction. In many cases, *Ea* resembles the literature *Em* values at early time points but is higher after a longer time in the light (Fig. 5, *Ea* box plots). This implies that, with time in the light, kinetic constraints change to favor the reduction of these proteins. Our in vivo observations are in line with earlier in vitro studies showing that some metabolites favor the reduction of target proteins by TRXs, such as FBP for cpFBPase 1 or the $NADPH/NADP^+$ ratio for NADP-MDH (*46*). FBP was shown to have an effect on cpFBPase in the low concentration range (*46*), which is coherent with $Ea_{cpFBPase}$ increasing only between darkness and 1.7 min of light (Fig. 5B). NADP-MDH shows a constant *Ea* for both its reductions, the first one being at equilibrium with TRXf (Table 2). The second reduction, which is responsible for the largest activity increase (*74*), is the one subject to inhibition at low $NADPH/(NADP^+ + NADPH)$ ratios (*46*, *67*) and with a higher *Ea* than measured in vitro (Fig. 2). A correlation between NADP-MDH activity and the reduced state of NADP, with both showing a transient increase during photosynthesis induction, has also been previously documented (*34*, *67*). These results would explain the stable *Ea* for the second reduction, if the $NADPH/NADP^+$ ratio would not drop below the inhibiting threshold in our conditions. Nevertheless, regulation by the redox state of NADP cannot explain why *Ea* is higher than the *Em* measured in vitro. Modulation of posttranslational redox regulation by metabolites was proposed to be a general mechanism for the individual fine-tuning of enzyme activities (*9*). The steady-state *Ea* values differ between enzymes in our study, as do the extent and timing of *Ea* value changes. Thus, the redox network at a given time

point cannot result from common constraints in the reactions of target proteins with TRXf.

Apart from metabolites, other parameters can kinetically influence the reduction of enzymes. Redox equilibration between photosynthetic TRXs and their targets can be slow if structural constraints hinder physical interaction, as in the case of poor electrostatic complementarity between TRXs and targets. Another well-described example is the supercomplex that is quickly formed by PRK, GAPDH, and chloroplast protein 12 in the dark, inactivating PRK and GAPDH irrespective of their redox states and preventing interaction of PRK with TRXs (*75*, *76*). Since GAPB and PRK are oxidized in the dark (Fig. 5, A and D) and the supercomplex is hardly found in tobacco (*77*), this regulation of PRK and GAPDH activities might remain limited in this species. Another parameter that can influence the redox state of enzymes is the stromal Mg^{2+} concentration, which could itself be redox-regulated through MGT10. Several of the *Ea*-changing redox-regulated enzymes have been shown to require ~2 to 10 mM Mg^{2+} for optimal activity (*10*, *70*). For cpFBPase and SBPase, the magnesium dependence is explained by the complexes Mg^{2+}-FBP and Mg^{2+}-SBP being the true substrates of the enzymes (*69*, *71*). The mechanism of the increase in Mg^{2+} has remained enigmatic because of the believed lumenal origin of the magnesium ions in the absence of an identifiable specific Mg^{2+} transporter in the thylakoid membrane (*78*) and in view of the low permeability of the chloroplast envelope to Mg^{2+} (*79*). The function of MGT10 is associated with chloroplast biogenesis (*80*, *81*), and its redox regulation would fit with both photosynthesis regulation and chlorophyll biosynthesis (*82*). The presence of a Mg^{2+} transporter in the envelope would allow partial uncoupling of Mg-requiring stromal reactions occurring in the light from regulation of the pmf across the thylakoid membrane. More work will be needed to investigate the role of the redox regulation of MGT10 in the control of the stromal Mg^{2+} concentration.

Redox-regulated enzymes thus have multiple mechanisms that regulate their activation upon dark-to-light transition, including redox control of their activity, which itself can be regulated, and direct regulation of enzyme activity by metabolites, the ionic milieu, or other factors. The dominant level of regulation is specific to each enzyme. It can be envisaged that the presence of multiple layers of regulation increases flexibility and facilitates adjustment of flux at each step of the cycle, in steady state and, even more importantly, under fluctuating conditions. Because of the extremely rapid flux in the CBC and the small sizes of the CBC metabolite pools, turnover times of the CBC metabolites are very fast, often well under 1 s (*51*, *83*). A small difference in flux at different steps in the pathway, therefore, can rapidly lead to accumulation of metabolites in one part of the CBC and depletion in another, causing serious impairment of flux through the entire pathway. Sensitive modulation of redox activation by the levels of substrates, products, and allosteric regulators likely provides a powerful and flexible mechanism to maintain fluxes in balance in the entire CBC. This has already been suggested on the basis of cpFBPase 1 and NADP-MDH (*9*, *84*) but could be a more general principle for proteins with changing *Ea* values.

MATERIALS AND METHODS

Plant material and growth conditions

Tobacco wild-type plants (*N. tabacum* cv. Petit Havana) were grown on a soil-vermiculite mixture (2:1) in a controlled environment chamber under a diurnal cycle of 18 hours of ~40 μmol photons m^{-2} s^{-1} light (red, blue, far red, and mostly white light-emitting diodes) at 22°C and 6 hours of darkness at 18°C. Relative humidity was set to 75%. All samples were taken from leaf #5 (numbering from the bottom of the plant, excluding the cotyledons) of eight-leaf plants, which corresponded to the youngest fully expanded leaf.

Sampling for proteomics

Three biological replicates were analyzed and harvested from three independent plant cultures. At 9 hours after the onset of light, four plants were put in darkness for 30 to 45 min to allow light-dependent processes to reset. Four discs (2.5 cm diameter) were harvested along the length of one-half of each leaf number 5 (Fig. 1). One sample consisted of four leaf discs, each of them coming from a different plant and a different position on the base-to-tip internal leaf developmental gradient. The discs were then placed onto a humid Whatman paper and treated with 0 s (tp0), 30 s (tp1), 100 s = 1.7 min (tp2), or 10 min (tp3) of growth light. At the end of the treatment, the leaf juice was rapidly extracted from the discs following published procedures (*12*). Four leaf discs produced ~100 μl of juice drops, which fell directly into 900 μl of ice-cold trichloroacetic acid [TCA; 10% (m/v) final concentration], leading to precipitation of the proteins and protonation of the thiolate groups of reduced cysteines. The time between the end of the light treatment and the juice expression was around 10 s (in vivo conditions), and the time for juice droplets to fall into TCA did not exceed 1 s.

Labeling

Samples for proteomic analyses were labeled according to published protocols (*64*). Briefly, TCA-precipitated material was split into two tubes of 450 μl each. The tubes were centrifuged, and the pellets were washed twice with cold acetone, then resuspended in 1 ml of urea buffer [8 M urea, 100 mM tris-HCl (pH 7.9), 1 mM EDTA, 2% SDS, and Roche protease inhibitor cocktail] complemented with 50 mM *N*-ethylmaleimide (NEM), and incubated for 2 hours at room temperature in the dark. The first tube then received 110 μl of cold 100% TCA and was stored on ice (control), whereas 110 μl of 1 M dithiothreitol (DTT) was added to the second tube, which was left for an additional hour at room temperature in the dark. Cold 100% TCA (121 μl) was then added to the second tube, and both tubes were centrifuged; the precipitated pellets were washed with ethanol and resuspended in 50 μl of urea buffer complemented with Mal-PEG at a final concentration of 10 mM. The tubes were incubated for 2 hours at room temperature with gentle shaking. Hence, reduced cysteines at the time of harvest were bound to small-sized NEM, while any oxidation of the cysteines that would be reversed by DTT (particularly disulfide bonds) resulted in the binding to large-sized Mal-PEG. In the control samples, oxidized cysteines remained unlabeled by Mal-PEG, thus keeping the molecular weights of the proteins very similar to those of the proteins with NEM-labeled reduced cysteines. In the next step, only the control corresponding to tp0 was analyzed and called tpc. Samples were fully reduced and denatured by adding sample buffer [final concentrations: 10% glycerol, 1% SDS, 50 mM 2-mercaptoethanol, 15 mM DTT, 75 mM tris-HCl (pH 6.8), 1 mM EDTA, and pyronin Y], followed by incubation for 1 hour at room temperature.

Sample quality control and peptide preparation

Fifty micrograms of protein was loaded on 10% SDS-polyacrylamide NuPAGE (Invitrogen) gels and separated 2 hours at 100 V with

Mops buffer. After transfer on polyvinylidene difluoride membranes, a Western blot was performed with the anti-FBPase antibody to check the quality of the samples (Fig. 1 and fig. S1). For sample preparation, aliquots of 100 µg of protein were loaded on 10% SDS-polyacrylamide NuPAGE (Invitrogen) gels (one gel per replicate with randomized sample order to minimize positional effects) and separated as above. Gels were stained in Coomassie Blue solution [20% (v/v) methanol, 10% (v/v) acetic acid, and 0.1% (m/v) Coomassie Brilliant Blue R] for 45 min and then destained twice in 10% (v/v) methanol and 5% (v/v) acetic acid for 1 hour at room temperature. Each lane of the gel was cut into eight fractions corresponding to the following molecular weight ranges: fraction 1, ~130 kDa and above; fraction 2, ~80 to ~130 kDa; fraction 3, ~55 to ~80 kDa; fraction 4, ~50 to ~55 kDa (mainly containing the large subunit of Rubisco); fraction 5, ~40 to ~50 kDa; fraction 6, ~26 to ~40 kDa; fraction 7, ~18 to ~26 kDa; and fraction 8, ~18 kDa and below (Fig. 1). The resulting 120 gel pieces were treated with the HiT-Gel method for protein digestion (*85*).

Liquid chromatography and mass spectrometric analysis

MS samples were prepared as described in (*85*) with minor modifications. Briefly, peptides were resuspended in 40 µl of 3% (v/v) acetonitrile and 0.1% (v/v) formic acid. Measurements were performed on a Q Exactive Plus mass spectrometer coupled to an nLC100 nano-HPLC (Thermo Fisher Scientific). Eight microliters of the samples was loaded onto an Acclaim PepMap100 reversed phase column (75 µm inner diameter, 15 cm length, and 2 µm bead size; Thermo Fisher Scientific) and eluted with a 3 to 40% (v/v) acetonitrile concentration gradient over 70 min. The column was then washed with 80% (v/v) acetonitrile for 10 min at a flow rate of 0.25 µl/min. Peptide ions were detected in a full MS1 scan for mass-to-charge ratios between 300 and 1600. MS2 scans were performed for the 15 peptides with the highest MS signal (minimal signal strength, 500 hits; isolation width mass-to-charge ratio, 2 *m*/*z*; and relative collision energy, 35%). Precursor masses for which tandem MS (MS/MS) spectra had been recorded were excluded from further MS/MS scans for 20 s. The MS proteomics data have been deposited to the ProteomeXchange Consortium via the PRIDE (*86*) partner repository with the dataset identifier PXD025217.

Data analysis

Construction of the POTbase and sPOTbaseMS databases

Construction of the POTbase from HOMs and ORTHOs. Protein coding sequences for all land plants included in PLAZA 2.5 (*87*) were downloaded and combined with protein coding sequences derived from the potato and tomato genome project (*Solanum tuberosum* and *Solanum lycopersicum*, respectively) along with protein sequences from *Brassica rapa* (*88*–*90*). Homologous gene families and orthologous groups (HOMs and ORTHOs) were generated using BLAST+ (*91*) with tribeMCL (*92*) and OrthoMCL (*93*), respectively, as described in (*87*). Available tobacco protein sequences from *Nicotiana sylvestris* (Nsyl) and *Nicotiana tomentosiformis* (Ntom) (*94*) and tobacco organellar proteins (NC_006581.1 and NC_001879.2) were assigned to HOMs and ORTHOs by BLAST as described in (*95*) and on https://chlorobox.mpimp-golm.mpg.de/potbase_ms.html. The resulting clusters were named POTs (Putative Orthologs of Tobacco) and the corresponding MS-database POTbaseMS (*96*).

Subclustering of POTbaseMS into sPOTbaseMS. For our study, the definition of the POTs was not precise enough, since several known redox-regulated proteins (e.g., GAPB subunit of GAPDH, APS subunit of AGPase, and plastid NADP-MDH) belonged to the same POTs as their non–redox-regulated homologs (GAPDH subunit A and AGPase large subunit, MDH of other compartments). Subclustering of the POTs in smaller protein groups was thus necessary, resulting in subPOTs (sPOTs) that are more representative of functionally or regulatory meaningful units. Therefore, most subPOTs can be referred to as proteins. The basis for subclustering POTs was POTbaseMS 0.8, for which several POTs had already been curated manually [see https://chlorobox.mpimp-golm.mpg.de/potbase-application.html and (*96*)]. All POTs that did not undergo manual curation were subjected to the following procedure. For each POT, the sequences of *N. sylvestris*, *N. tomentosiformis*, *S. lycopersicum*, and *A. thaliana* were collected and aligned by MUSCLE v3.8.31 (with parameter "-diags"). Subsequently, the MUSCLE alignment was submitted to GBLOCKS 0.91b (with parameters "-d=y -e=GBL -t=p -b5=h -b4=5"). The sequences trimmed by GBLOCKS were used for further processing if the new number of amino acid positions exceeded 50 and more than 33.3% of the original positions were kept. Otherwise, the MUSCLE alignment was used for further processing. The MUSCLE alignments labeled by GBLOCKS are accessible at https://chlorobox.mpimp-golm.mpg.de/potbase-application.html. The sequences of each POT were sent to USEARCH v8.1.1861 for agglomerative clustering ("-cluster_agg") into sPOTs by single linkage (-linkage min), whereby the sequences of POTs curated by GBLOCKS and noncurated POTs were submitted with identity thresholds "-id 0.9" and "-id 0.7," respectively.

Quantification, normalization, and identification of oxidized and reduced fraction clusters

Data processing. Quantitative analysis of MS/MS measurements was performed using MaxQuant 1.6.0.16 (*97*). Searches were performed using a spectral library based on the sPOTbaseMS database. Library construction considered methionine oxidation and acetylation of protein N termini as variable and carbamidomethylation of cysteines as a fixed modification. False discovery rate thresholds for peptide spectrum matches and protein identification were set to 1%. Ion species mapping to contaminants were excluded, and peptide species identified at multiple charge states were aggregated by summing their intensities. According to the assumption that identical protein amounts were used, peptide intensities were normalized for each lane, using the median intensity of all identified peptides per replicate. Subsequently, peptides were aggregated according to their assigned protein group. Because of the potentially different ionization efficiencies among cysteine-containing peptides modified by NEM and PEG, we excluded them from protein quantification. We optimized the respective quantile of peptide intensities for protein quantification resulting in the most stable quantification judged by minimal replicate dispersion.

Identification of redox clusters. To quantify the redox state of a single protein, the data were ordered in a matrix that reflects the protein gel (Fig. 1). Under the assumption that two lanes showing the most negative linear correlation are most likely to house the oxidized and reduced forms of the respective protein, the row-wise covariance matrix of the data matrix was computed. On the basis of this matrix, the pair of rows with the highest anticorrelation was identified and used as seed for a subsequent clustering procedure. This step was included to aggregate proteins that are distributed unevenly across different gel fractions. Lanes above, below, and between the oxidized and reduced seeds were considered to

potentially harbor protein material belonging to either one of the redox states. To select fractions whose sums account for the protein abundance at a time point, we chose to maximize the anticorrelation between redox pairs. This was achieved by computing the covariance of all possible combinations of fractions with the respective seeds when compared to the seed of the corresponding redox state. Lanes that were adjacent to both seeds and proteins showing no anticorrelation were discarded from downstream analysis.

Replicate pruning. The workflow described above was carried out independently for every biological replicate. After identification of clusters, replicates were grouped by proteins and replicate statistics were calculated. This included measures for dispersion (coefficient of variation) for the seed fractions solely and for the optimized cluster. These estimators were subsequently used to examine whether the clustering procedure increased the fraction of noise in the recorded kinetics. If an increase of the latter was detected, only the seed fractions were retained.

Missing value imputation. Missing values were imputed at the protein level before calculating replicate statistics. Where possible, we used mean value imputation adding random Gaussian noise estimated using sample mean and variance. Otherwise, the missing value imputation was based on the 0.2 quantile of the empirical distribution of the experiment, simulating the detection limit for lowly abundant proteins.

Statistical identification and classification of redox regulation

On the basis of our experimental design, we classified the proteins into (i) "nonredox" (proteins with no or only reduced cysteines), (ii) Oxidized Cys (proteins with oxidized cysteines in the dark), and (iii) Light responsive (proteins with oxidized cysteines in the dark showing a change of redox state in the light) using a rule-based classification evaluating a combination of statistically significant changes. The set of our classification rules were learned from the behaviors of 10 well-known measured candidate proteins (cpFBPase, SBPase, PRK, GAPB, G6PD1, APS1, ATPC1, NADP-MDH, TRXf, and PGRL1). To be classified as Oxidized Cys proteins, candidates needed to fulfill the requirement that the level of oxidized protein increases and the reduced form decreases from tpc to tp0, while also being reproducibly quantified over the time course. Oxidized Cys proteins were additionally classified as Light-responsive proteins if their reduced and oxidized fractions anticorrelated while showing a statistically significant change in abundance relative to the onset of light. Statistical significance was determined by one-way analysis of variance (ANOVA) adjusted for multiple testing and Hay's post hoc testing applied on each of the redox clusters and rest material. These conditions allowed us to retrieve 9 of the 10 candidates as temporally regulated. The only exception was cpFBPase 1, showing a temporal response but not retrieved after our filters, probably because of its noisy replicates. In addition, quality metrics such as the number of imputed values, identified seeds, clusters, and their indices were reported.

Apparent midpoint redox potential (Ea) calculation and evaluation of the equilibrium between TRXf and other proteins

Theoretical considerations. If a protein X, showing a change in its redox state, is at equilibrium with TRXf, the quotient (Q) of the reaction in Eq. 1 below should be equal to the equilibrium constant K, which can be written following the Nernst equation, Eq. 2

$$\mathrm{TRXf_{red}} + \mathrm{X_{ox}} \xrightarrow{2\,e^-} \mathrm{TRXf_{ox}} + \mathrm{X_{red}} \quad (1)$$

$$Q = \frac{[\mathrm{X_{red}}]*[\mathrm{TRXf_{ox}}]}{[\mathrm{X_{ox}}]*[\mathrm{TRXf_{red}}]} = K = 10^{(Em_X - Em_{\mathrm{TRXf}})*\frac{2F}{RT}} \quad (2)$$

Thus, at each time point t

$$(Ea_X - Em_{\mathrm{TRXf}})(t) = 30\ \mathrm{mV} * \log\left(\frac{[X_{red}](t)*[\mathrm{TRXf_{ox}}](t)}{[X_{ox}](t)*[\mathrm{TRXf_{red}}](t)}\right) \quad (3)$$

where Ea_X is the apparent Em of protein X. If the hypothesis of equilibrium is met, $Ea_X = Em_X$, with Em_X being the redox potential of protein X.

We also have $[\mathrm{TRXf_{red}}](t) = [\mathrm{TRXf}] * TRXf_{red}(t)$ and $[\mathrm{TRXf_{ox}}](t) = [\mathrm{TRXf}] * TRXf_{ox}(t) = [\mathrm{TRXf}] * (1 - TRXf_{red}(t))$, where [TRXf] is the total concentration of TRXf that does not depend on time, and $TRXf_{ox}(t)$ and $TRXf_{red}(t)$ are the proportions of reduced and oxidized forms of TRXf at each time point t.

Integrating this in Eq. 3, we obtain

$$(Ea_X - Em_{\mathrm{TRXf}})(t) = 30\ \mathrm{mV} * \log\frac{\frac{1}{TRXf_{red}(t)} - 1}{\frac{X_{ox}(t)}{X_{red}(t)}} \quad (4)$$

or using the redox proportions of X

$$(Ea_X - Em_{\mathrm{TRXf}})(t) = 30\ \mathrm{mV} * \log\frac{\frac{1}{TRXf_{red}(t)} - 1}{\frac{1}{X_{red}(t)} - 1} \quad (5)$$

Selection of proteins of interest. The analysis was performed on the proteins classified as light-dependent redox-regulated excluding all the non-stromal proteins, for which it is meaningless to evaluate their equilibrium with TRXf, and PGRL1 (POT003083_1; see the next paragraph).

Normalization of protein abundance. To obtain the proportions of reduced proteins, we first normalized the reduced cluster values to the maximum value of each replicate. Normalizing to the maximum of the replicate instead of tpc allows the reduced proportion to not be above 1 for kinetics that reach ~100% reduction, which would prevent the application of Eq. (5). It also allows us to remove replicate effects in the abundance levels, if present. This calculation is possible for all proteins where the reduced and oxidized clusters gather the majority of the protein material. For TRXf, the rest material represents a non-negligible amount of the protein (Fig. 3) but contains mostly oxidized forms (Fig. 2 and data file S3, POT006052, tpc < tp0 for fractions 2, 3 and 4). We can thus assume that $\mathrm{TRXf_{ox}} = 1 - \mathrm{TRXf_{red}}$ and apply Eq. (5). For PGRL1, which has numerous redox active cysteines (*98*), the amount of unclustered material represents the majority of the protein at all time points (Fig. 2), and therefore, the protein was excluded from this part of the study. Last, NADP-MDH has three redox forms, which contain zero, one, and two disulfide bonds and correspond to two redox reactions (two to one bond and one to zero bond) (*43*). These three forms were measured separately in fractions 5, 3, and 2, respectively. In our cluster analysis, both oxidized (fraction 2) and reduced (fraction 5) clusters show significant differences (at $P < 0.05$) over time, as well as the rest material (containing not only fraction 3 but also the minor fractions 1, 4, and 6, depending on the replicate) (POT005226_3;

Fig. 2 and data file S3). To calculate the proportions of each form to be used in Eq. 4 for both redox reactions, only the amounts measured in fractions 2, 3, and 5 were used. For each replicate, the fraction 2 and 3 amounts at the control time point were subtracted from all the other time point values of these fractions, and the proportions of the three forms were then calculated at each time point. These are the kinetics presented in Fig. 4 for NADP-MDH.

Calculation of Em differences. Equation 4 (for NADP-MDH) and Eq. 5 (for all other proteins) were used to calculate the $Ea_X - Em_{TRXf}$ differences. For each time point, all pairs of the three replicates of TRXf and the proportions of protein X were used, which averaged out the potential replicate effects on the kinetics. Proportions coming from two or more imputed missing values of either TRXf or protein X were removed, which resulted in completely removing tp0 (three missing TRXf values), leaving the total number of differences for each protein X between 18 and 27 (nine values for three time points).

Statistics. Statistical significance of the $Ea_X - Em_{TRXf}$ differences between time points was determined using one-way ANOVA ($P \leq 0.05$) with previous outlier filtering according to Tukey's interquantile method.

Comparison of Ea with Em literature values. For the proteins for which equality was checked, *Ea* was estimated by adding $Em_{TRXf} = -290$ mV to the average of $Ea_X - Em_{TRXf}$ differences calculated over all time points. (All redox potential values given in this work hold true at pH 7.) The Em_{TRXf} value has not been measured in tobacco, but in several other plants, and appears quite constant (*38*). The *Ea* values were then compared to available measurements of *Em* in the literature, and *Ea* was declared equal to *Em* when the literature value was closer than one-half of the calculated SD from the mean *Ea*.

Modeling the kinetic behavior of proteins at equilibrium with TRXf. From Eq. 5, we obtain the reduced proportion of a protein X of redox potential Em_X at equilibrium with TRXf in Eq. 6

$$X_{red}(t) = \frac{C * TRXf_{red}(t)}{1 - TRXf_{red}(t) + C * TRXf_{red}(t)} \quad (6)$$

where $C = 10^{\frac{(Em_X - Em_{TRXf})}{30\ mV}}$.

This equation was applied for virtual proteins with *Em* ranging from −220 to −330 mV, using $Em_{TRXf} = -290$ mV and the calculated reduced proportions of TRXf in the different time points, and $TRXf_{red}(tp0) = 0$.

Metabolite measurements

Samples for metabolite measurements were harvested in the middle of the day, either directly from the growth light condition ("L"), after transfer to the dark for 30 min ("D"), or in the growth light for 100 s after 30 min in the dark ("1.7"). Plant material was ground to a fine powder in a cryo-robot (*99*) and stored at −80°C. Metabolites were extracted and quantified by liquid chromatography (LC)–MS/MS (*83*). All samples were spiked with stable isotope-labeled internal standards for correction of ion suppression and other matrix effects (*100*). 3PGA gives a broad, poorly defined peak in LC-MS/MS and was therefore quantified enzymatically, as well as ATP (*101*). For further calculations, measured metabolite contents in nmol/gFW (gram fresh weight) were converted in nmol/mg chlorophyll using the content of chlorophyll measured in the same samples (around 0.8 mg of chlorophyll/gFW). Stromal metabolite concentrations were then obtained using the chlorophyll mass–to–stromal volume relationship (*102*), correcting the measured contents for multiple subcellular localizations when needed (*51*, *103*). Data for changing proportions between plastid and extraplastidic compartments during photosynthesis induction in similar CO_2 assimilation kinetic conditions were only available for FBP.

We used the metabolite and CO_2 assimilation measurements to estimate changes in the redox proportions of the three enzymes catalyzing the irreversible reactions of the CBC, namely, PRK, cpFBPase, and SBPase. The reaction rate catalyzed by an enzyme present under two differently active redox forms can be written as the sum of their respective rates, given by Eq. 7

$$v = E * \left(P_{red} * kcat_{red} * \frac{\prod_i (Si/K_{Mi,red})^{mi}}{1 + \prod_i (Si/K_{Mi,red})^{mi}} + P_{ox} * kcat_{ox} * \frac{\prod_i (Si/K_{Mi,ox})^{mi}}{1 + \prod_i (Si/K_{Mi,ox})^{mi}}\right) \quad (7)$$

where E is the total enzyme concentration (assumed constant during our experiment), P is the proportion of a redox form, *kcat* is its catalytic constant, *Si* is the concentration of substrate *i*, *mi* is its stoichiometric coefficient in the catalyzed reaction, and K_{Mi} is its Michaelis-Menten constant for the considered redox form. Measured competitive inhibitors of the enzymes [F6P for cpFBPase (*69*) and RuBP for PRK (*54*)] were neglected because of their very low concentration over K_I ratios in our conditions.

For the three considered enzymes, the contribution of the oxidized form to the total activity can be neglected. For cpFBPase, K_{Mox} is 20 times smaller than K_{Mred} (*104*), making the ratio $[FBP]/K_{MFBPox}$ reach a maximum value of ~0.005 at the maximum measured FBP concentration. For SBPase and PRK, the main difference between both redox forms lies in the *kcat*, which is 100 and 40 times, respectively, lower for the oxidized form than for the reduced one, although SBPase also has a fourfold decreased K_M when reduced (*104*, *105*). Considering the two time points at 1.7 min and steady-state light, one can thus find the ratio of the reduced proportions between these two time points in Eq. 8

$$\frac{Pred(1.7)}{Pred(ss)} = \frac{v(1.7)}{v(ss)} * \frac{\prod_i Si(ss)^{mi}}{\prod_i Si(1.7)^{mi}} * \frac{1 + \prod_i (Si(1.7)/K_{Mi})^{mi}}{1 + \prod_i (Si(ss)/K_{Mi})^{mi}} \quad (8)$$

The K_Ms of the reduced enzymes for ATP and Ru5P (PRK), FBP (cpFBPase), and SBP (SBPase) were retrieved from the literature (*104*–*106*). Although these values might not be valid in vivo or for tobacco enzymes, the maximal measured substrate concentrations remain one to two orders of magnitude below their K_Ms, and the term using these K_Ms thus only brings a minor correction to the result. Fluxes through the pathway [$v(1.7)$ and $v(ss)$] were estimated by CO_2 assimilation, assuming that respiration and photorespiration rates do not change between 1.7 min and steady-state light.

Fluorescence and gas exchange measurements

Chlorophyll fluorescence and gas exchange were measured in vivo with a GFS-3000 open gas-exchange system equipped with the light-emitting diode array unit 3056-FL as actinic light source (Heinz Walz GmbH). Two measurements were performed on both sides of leaf #5

of eight-leaf plants (surface, 8 cm^2), with an actinic red light set at 10 µmol photons m^{-2} s^{-1} (yielding the same kinetics of CO_2 assimilation as the growth light), at 22°C, 17,500 µl $liter^{-1}$ humidity, and 400 ppm (parts per million) CO_2, after a dark adaptation of 30 to 45 min. Two minutes before the onset of light, a saturating light pulse (400 ms, 10,000 µmol photons m^{-2} s^{-1}) was applied, which allowed the measurement of the Fv/Fm ratio and ensured that it was the same for both samples. CO_2 assimilation and stationary fluorescence were measured every second for 3 min and then every 10 s for the next 7 min on the sample without saturating pulses. On the sample used for calculating fluorescence parameters, saturating pulses (400 ms, 10000 µmol photons m^{-2} s^{-1}) were applied every 14 s for the first 4 min starting 1 s after the onset of light and then every minute for the next 7 min. CO_2 assimilation and stationary fluorescence were measured every second starting 5 s after the saturating pulses for the first 4 min and then every 10 s. Maximum fluorescence was recorded after each saturating pulse. Yield of PSII, NPQ, and 1 − qL were then calculated (*107*). All measurements were recorded on four plants and are presented in fig. S2. For clarity, only the data corresponding to the representative WT1 are displayed in Fig. 3.

Structure and sequence analyses

Structures of tobacco cpFBPase 1 (POT004591_2), cpFBPase 2 (POT004591_1), cytFBPase (POT000761_1), and MGT10 (POT007907) were modeled using I-TASSER (*108*). Sequences of their homologs in other organisms were retrieved by blasting the protein sequences against the National Center for Biotechnology Information or the Phytozome databases. Sequences were aligned with MAFFT v7.409 (*109*). IDs of the sequences are listed in table S3.

SUPPLEMENTARY MATERIALS

Supplementary material for this article is available at https://science.org/doi/10.1126/sciadv.abi8307

View/request a protocol for this paper from *Bio-protocol*.

REFERENCES AND NOTES

1. Y. Gibon, O. E. Blaesing, J. Hannemann, P. Carillo, M. Höhne, J. H. M. Hendriks, N. Palacios, J. Cross, J. Selbig, M. Stitt, A robot-based platform to measure multiple enzyme activities in Arabidopsis using a set of cycling assays: Comparison of changes of enzyme activities and transcript levels during diurnal cycles and in prolonged darkness. *Plant Cell* **16**, 3304–3325 (2004).
2. H. W. Heldt, L. Rapley, Specific transport of inorganic phosphate, 3-phosphoglycerate and dihydroxyacetonephosphate, and of dicarboxylates across the inner membrane of spinach chloroplasts. *FEBS Lett.* **10**, 143–148 (1970).
3. J. Selinski, R. Scheibe, Malate valves: Old shuttles with new perspectives. *Plant Biol. Stuttg. Ger.* **21** (Suppl 1), 21–30 (2019).
4. S. K. Mühlbauer, L. A. Eichacker, Light-dependent formation of the photosynthetic proton gradient regulates translation elongation in chloroplasts. *J. Biol. Chem.* **273**, 20935–20940 (1998).
5. A. N. Dodd, J. Kusakina, A. Hall, P. D. Gould, M. Hanaoka, The circadian regulation of photosynthesis. *Photosynth. Res.* **119**, 181–190 (2014).
6. K. B. Busch, G. Deckers-Hebestreit, G. T. Hanke, A. Y. Mulkidjanian, Dynamics of bioenergetic microcompartments. *Biol. Chem.* **394**, 163–188 (2013).
7. F. Chaux, G. Peltier, X. Johnson, A security network in PSI photoprotection: Regulation of photosynthetic control, NPQ and O_2 photoreduction by cyclic electron flow. *Front. Plant Sci.* **6**, 875 (2015).
8. A. U. Igamberdiev, L. A. Kleczkowski, Thermodynamic buffering, stable non-equilibrium and establishment of the computable structure of plant metabolism. *Prog. Biophys. Mol. Biol.* **146**, 23–36 (2019).
9. J. Knuesting, R. Scheibe, Small molecules govern thiol redox switches. *Trends Plant Sci.* **23**, 769–782 (2018).
10. W. A. Laing, M. Stitt, H. W. Heldt, Control of CO_2 fixation. Changes in the activity of ribulosephosphate kinase and fructose-and sedoheptulose-bisphosphatase in chloroplasts. *Biochim. Biophys. Acta BBA Bioenerg.* **637**, 348–359 (1981).
11. E. Latzko, R. von Garnier, M. Gibbs, Effect of photosynthesis, photosynthetic inhibitors and oxygen on the activity of ribulose 5-phosphate kinase. *Biochem. Biophys. Res. Commun.* **39**, 1140–1144 (1970).
12. W. Wirtz, M. Stitt, H. W. Heldt, Light activation of Calvin cycle enzymes as measured in pea leaves. *FEBS Lett.* **142**, 223–226 (1982).
13. H. Ziegler, I. Ziegler, Der Einfluß der Belichtung auf die $NADP^+$-abhängige Glycerinaldehyd-3-phosphat-Dehydrogenase. *Planta* **65**, 369–380 (1965).
14. B. B. Buchanan, Role of light in the regulation of chloroplast enzymes. *Annu. Rev. Plant Physiol.* **31**, 341–374 (1980).
15. K. Lendzian, H. Ziegler, Über die Regulation der Glucose-6-phosphat-Dehydrogenase in Spinatchloroplasten durch Licht. *Planta* **94**, 27–36 (1970).
16. J. H. M. Hendriks, A. Kolbe, Y. Gibon, M. Stitt, P. Geigenberger, ADP-glucose pyrophosphorylase is activated by posttranslational redox-modification in response to light and to sugars in leaves of Arabidopsis and other plant species. *Plant Physiol.* **133**, 838–849 (2003).
17. B. Naranjo, A. Diaz-Espejo, M. Lindahl, F. J. Cejudo, Type-f thioredoxins have a role in the short-term activation of carbon metabolism and their loss affects growth under short-day conditions in Arabidopsis thaliana. *J. Exp. Bot.* **67**, 1951–1964 (2016).
18. I. Thormählen, J. Ruber, E. von Roepenack-Lahaye, S.-M. Ehrlich, V. Massot, C. Hümmer, J. Tezycka, E. Issakidis-Bourguet, P. Geigenberger, Inactivation of thioredoxinf1 leads to decreased light activation of ADP-glucose pyrophosphorylase and altered diurnal starch turnover in leaves of Arabidopsis plants. *Plant Cell Environ.* **36**, 16–29 (2013).
19. K. Yoshida, T. Hisabori, Determining the rate-limiting step for light-responsive redox regulation in chloroplasts. *Antioxidants* **7**, 153 (2018).
20. M. Balsera, E. Uberegui, P. Schürmann, B. B. Buchanan, Evolutionary development of redox regulation in chloroplasts. *Antioxid. Redox Signal.* **21**, 1327–1355 (2014).
21. K. Yoshida, Y. Matsuoka, S. Hara, H. Konno, T. Hisabori, Distinct redox behaviors of chloroplast thiol enzymes and their relationships with photosynthetic electron transport in *Arabidopsis thaliana*. *Plant Cell Physiol.* **55**, 1415–1425 (2014).
22. J. M. Pérez-Ruiz, B. Naranjo, V. Ojeda, M. Guinea, F. J. Cejudo, NTRC-dependent redox balance of 2-Cys peroxiredoxins is needed for optimal function of the photosynthetic apparatus. *Proc. Natl. Acad. Sci. U.S.A.* **114**, 12069–12074 (2017).
23. M.-J. Vaseghi, K. Chibani, W. Telman, M. F. Liebthal, M. Gerken, H. Schnitzer, S. M. Mueller, K.-J. Dietz, The chloroplast 2-cysteine peroxiredoxin functions as thioredoxin oxidase in redox regulation of chloroplast metabolism. *eLife* **7**, e38194 (2018).
24. K. Yoshida, A. Hara, K. Sugiura, Y. Fukaya, T. Hisabori, Thioredoxin-like2/2-Cys peroxiredoxin redox cascade supports oxidative thiol modulation in chloroplasts. *Proc. Natl. Acad. Sci. U.S.A.* **115**, E8296–E8304 (2018).
25. K. Yoshida, T. Hisabori, Two distinct redox cascades cooperatively regulate chloroplast functions and sustain plant viability. *Proc. Natl. Acad. Sci. U.S.A.* **113**, E3967–E3976 (2016).
26. P. Geigenberger, I. Thormählen, D. M. Daloso, A. R. Fernie, The unprecedented versatility of the plant thioredoxin system. *Trends Plant Sci.* **22**, 249–262 (2017).
27. L. Martins, J. A. Trujillo-Hernandez, J.-P. Reichheld, Thiol based redox signaling in plant nucleus. *Front. Plant Sci.* **9**, 705 (2018).
28. I. M. Møller, A. U. Igamberdiev, N. V. Bykova, I. Finkemeier, A. G. Rasmusson, M. Schwarzländer, Matrix redox physiology governs the regulation of plant mitochondrial metabolism through posttranslational protein modifications. *Plant Cell* **32**, 573–594 (2020).
29. P. Geigenberger, A. R. Fernie, Metabolic control of redox and redox control of metabolism in plants. *Antioxid. Redox Signal.* **21**, 1389–1421 (2014).
30. B. P. Mooney, J. A. Miernyk, D. D. Randall, The complex fate of α-ketoacids. *Annu. Rev. Plant Biol.* **53**, 357–375 (2002).
31. D. R. Bergey, M. Orozco-Cardenas, D. S. de Moura, C. A. Ryan, A wound- and systemin-inducible polygalacturonase in tomato leaves. *Proc. Natl. Acad. Sci. U.S.A.* **96**, 1756–1760 (1999).
32. S. K. Pal, M. Liput, M. Piques, H. Ishihara, T. Obata, M. C. M. Martins, R. Sulpice, J. T. van Dongen, A. R. Fernie, U. P. Yadav, J. E. Lunn, B. Usadel, M. Stitt, Diurnal changes of polysome loading track sucrose content in the rosette of wild-type arabidopsis and the starchless *pgm* mutant. *Plant Physiol.* **162**, 1246–1265 (2013).
33. A. M. Gilmore, O. Björkman, Temperature-sensitive coupling and uncoupling of ATPase-mediated, nonradiative energy dissipation: Similarities between chloroplasts and leaves. *Planta* **197**, 646–654 (1995).
34. R. Scheibe, M. Stitt, Comparison of NADP-malate dehydrogenase activation, Q_A reduction and O_2 evolution in spinach leaves. *Plant Physiol. Biochem.* **26**, 473–481 (1988).
35. P. B. Lawrence, J. L. Price, How PEGylation influences protein conformational stability. *Curr. Opin. Chem. Biol.* **34**, 88–94 (2016).
36. R. P. Wulff, J. Lundqvist, G. Rutsdottir, A. Hansson, A. Stenbaek, D. Elmlund, H. Elmlund, P. E. Jensen, M. Hansson, The activity of barley NADPH-dependent thioredoxin reductase

C is independent of the oligomeric state of the protein: Tetrameric structure determined by cryo-electron microscopy. *Biochemistry* **50**, 3713–3723 (2011).
37. V. Collin, E. Issakidis-Bourguet, C. Marchand, M. Hirasawa, J.-M. Lancelin, D. B. Knaff, M. Miginiac-Maslow, The Arabidopsis plastidial thioredoxins: new functions and new insights into specificity. *J. Biol. Chem.* **278**, 23747–23752 (2003).
38. M. Hirasawa, P. Schürmann, J. P. Jacquot, W. Manieri, P. Jacquot, E. Keryer, F. C. Hartman, D. B. Knaff, Oxidation-reduction properties of chloroplast thioredoxins, ferredoxin:thioredoxin reductase, and thioredoxin f-regulated enzymes. *Biochemistry* **38**, 5200–5205 (1999).
39. P. Schürmann, J.-P. Jacquot, Plant thioredoxin systems revisited. *Annu. Rev. Plant Physiol. Plant Mol. Biol.* **51**, 371–400 (2000).
40. K. Yoshida, S. Hara, T. Hisabori, Thioredoxin selectivity for thiol-based redox regulation of target proteins in chloroplasts. *J. Biol. Chem.* **290**, 14278–14288 (2015).
41. L. Tarrago, E. Laugier, M. Zaffagnini, C. H. Marchand, P. Le Maréchal, S. D. Lemaire, P. Rey, Plant thioredoxin CDSP32 regenerates 1-cys methionine sulfoxide reductase B activity through the direct reduction of sulfenic acid. *J. Biol. Chem.* **285**, 14964–14972 (2010).
42. M. Hirasawa, E. Ruelland, I. Schepens, E. Issakidis-Bourguet, M. Miginiac-Maslow, D. B. Knaff, Oxidation–reduction properties of the regulatory disulfides of sorghum chloroplast nicotinamide adenine dinucleotide phosphate–malate dehydrogenase. *Biochemistry* **39**, 3344–3350 (2000).
43. M. Miginiac-Maslow, J.-M. Lancelin, Intrasteric inhibition in redox signalling: Light activation of NADP-malate dehydrogenase. *Photosynth. Res.* **72**, 1–12 (2002).
44. G. Née, M. Zaffagnini, P. Trost, E. Issakidis-Bourguet, Redox regulation of chloroplastic glucose-6-phosphate dehydrogenase: A new role for f-type thioredoxin. *FEBS Lett.* **583**, 2827–2832 (2009).
45. A. L. Preiser, N. Fisher, A. Banerjee, T. D. Sharkey, Plastidic glucose-6-phosphate dehydrogenases are regulated to maintain activity in the light. *Biochem. J.* **476**, 1539–1551 (2019).
46. M. Faske, S. Holtgrefe, O. Ocheretina, M. Meister, J. E. Backhausen, R. Scheibe, Redox equilibria between the regulatory thiols of light/dark-modulated chloroplast enzymes and dithiothreitol: Fine-tuning by metabolites. *Biochim. Biophys. Acta* **1247**, 135–142 (1995).
47. G. P. Holbrook, S. C. Galasinski, M. E. Salvucci, Regulation of 2-carboxyarabinitol 1-phosphatase. *Plant Physiol.* **97**, 894–899 (1991).
48. M. A. Moxley, D. A. Beard, J. N. Bazil, A pH-dependent kinetic model of dihydrolipoamide dehydrogenase from multiple organisms. *Biophys. J.* **107**, 2993–3007 (2014).
49. D. Schimkat, D. Heineke, H. W. Heldt, Regulation of sedoheptulose-1,7-bisphosphatase by sedoheptulose-7-phosphate and glycerate, and of fructose-1,6-bisphosphatase by glycerate in spinach chloroplasts. *Planta* **181**, 97–103 (1990).
50. A. Tiessen, J. H. M. Hendriks, M. Stitt, A. Branscheid, Y. Gibon, E. M. Farré, P. Geigenberger, Starch synthesis in potato tubers is regulated by post-translational redox modification of ADP-glucose pyrophosphorylase: A novel regulatory mechanism linking starch synthesis to the sucrose supply. *Plant Cell* **14**, 2191–2213 (2002).
51. M. Stitt, W. Wirtz, H. W. Heldt, Metabolite levels during induction in the chloroplast and extrachloroplast compartments of spinach protoplasts. *Biochim. Biophys. Acta* **593**, 85–102 (1980).
52. D. M. Kramer, R. R. Wise, J. R. Frederick, D. M. Alm, J. D. Hesketh, D. R. Ort, A. R. Crofts, Regulation of coupling factor in field-grown sunflower: A redox model relating coupling factor activity to the activities of other thioredoxin-dependent chloroplast enzymes. *Photosynth. Res.* **26**, 213–222 (1990).
53. H. Konno, T. Nakane, M. Yoshida, H. Ueoka-Nakanishi, S. Hara, T. Hisabori, Thiol modulation of the chloroplast ATP synthase is dependent on the energization of thylakoid membranes. *Plant Cell Physiol.* **53**, 626–634 (2012).
54. A. Gardemann, M. Stitt, H. W. Heldt, Control of CO2 fixation. Regulation of spinach ribulose-5-phosphate kinase by stromal metabolite levels. *Biochim. Biophys. Acta BBA Bioenerg.* **722**, 51–60 (1983).
55. G. Capitani, Z. Marković-Housley, G. DelVal, M. Morris, J. N. Jansonius, P. Schürmann, Crystal structures of two functionally different thioredoxins in spinach chloroplasts. *J. Mol. Biol.* **302**, 135–154 (2000).
56. M. Chiadmi, A. Navaza, M. Miginiac-Maslow, J. P. Jacquot, J. Cherfils, Redox signalling in the chloroplast: Structure of oxidized pea fructose-1,6-bisphosphate phosphatase. *EMBO J.* **18**, 6809–6815 (1999).
57. J. Waese, J. Fan, A. Pasha, H. Yu, G. Fucile, R. Shi, M. Cumming, L. A. Kelley, M. J. Sternberg, V. Krishnakumar, E. Ferlanti, J. Miller, C. Town, W. Stuerzlinger, N. J. Provart, ePlant: Visualizing and exploring multiple levels of data for hypothesis generation in plant biology. *Plant Cell* **29**, 1806–1821 (2017).
58. S. Arrivault, T. Alexandre Moraes, T. Obata, D. B. Medeiros, A. R. Fernie, A. Boulouis, M. Ludwig, J. E. Lunn, G. L. Borghi, A. Schlereth, M. Guenther, M. Stitt, Metabolite profiles reveal interspecific variation in operation of the Calvin–Benson cycle in both C4 and C3 plants. *J. Exp. Bot.* **70**, 1843–1858 (2019).
59. R. Drummond, A. Tutone, Y.-C. Li, R. Gardner, A putative magnesium transporter AtMRS2-11 is localized to the plant chloroplast envelope membrane system. *Plant Sci.* **170**, 78–89 (2006).
60. L. Wang, D. Leister, L. Guan, Y. Zheng, K. Schneider, M. Lehmann, K. Apel, T. Kleine, The Arabidopsis SAFEGUARD1 suppresses singlet oxygen-induced stress responses by protecting grana margins. *Proc. Natl. Acad. Sci.* **117**, 6918–6927 (2020).
61. Arabidopsis Interactome Mapping Consortium, Evidence for network evolution in an Arabidopsis interactome map. *Science* **333**, 601–607 (2011).
62. X. Liu, S. R. Rodermel, F. Yu, A *var2* leaf variegation suppressor locus, SUPPRESSOR OF VARIEGATION3, encodes a putative chloroplast translation elongation factor that is important for chloroplast development in the cold. *BMC Plant Biol.* **10**, 287 (2010).
63. R. Nagarajan, K. S. Gill, Evolution of Rubisco activase gene in plants. *Plant Mol. Biol.* **96**, 69–87 (2018).
64. H. Peled-Zehavi, S. Avital, A. Danon, Methods of redox signaling by plant thioredoxins, in *Methods Redox Signal. Ed New Rochelle NY Mary Ann Liebert*, pp. 251–256 (2010).
65. P. Rey, S. Cuiné, F. Eymery, J. Garin, M. Court, J.-P. Jacquot, N. Rouhier, M. Broin, Analysis of the proteins targeted by CDSP32, a plastidic thioredoxin participating in oxidative stress responses. *Plant J. Cell Mol. Biol.* **41**, 31–42 (2005).
66. L. Nikkanen, J. Toivola, E. Rintamäki, Crosstalk between chloroplast thioredoxin systems in regulation of photosynthesis. *Plant Cell Environ.* **39**, 1691–1705 (2016).
67. C. H. Foyer, M. Lelandais, J. Harbinson, Control of the quantum efficiencies of photosystems I and II, electron flow, and enzyme activation following dark-to-light transitions in pea leaves: Relationship between NADP/NADPH ratios and NADP-malate dehydrogenase activation state. *Plant Physiol.* **99**, 979–986 (1992).
68. V. Ojeda, J. M. Pérez-Ruiz, F. J. Cejudo, 2-Cys peroxiredoxins participate in the oxidation of chloroplast enzymes in the dark. *Mol. Plant* **11**, 1377–1388 (2018).
69. A. Gardemann, D. Schimkat, H. W. Heldt, Control of CO_2 fixation regulation of stromal fructose-1,6-bisphosphatase in spinach by pH and Mg^{2+} concentration. *Planta* **168**, 536–545 (1986).
70. A. R. Portis, H. W. Heldt, Light-dependent changes of the Mg^{2+} concentration in the stroma in relation to the Mg^{2+} dependency of CO_2 fixation in intact chloroplasts. *Biochim. Biophys. Acta* **449**, 434–446 (1976).
71. I. E. Woodrow, D. J. Murphy, E. Latzko, Regulation of stromal sedoheptulose 1,7-bisphosphatase activity by pH and Mg^{2+} concentration. *J. Biol. Chem.* **259**, 3791–3795 (1984).
72. M. Stitt, J. Lunn, B. Usadel, Arabidopsis and primary photosynthetic metabolism—More than the icing on the cake. *Plant J.* **61**, 1067–1091 (2010).
73. H. Usuda, M. S. Ku, G. E. Edwards, Activation of NADP-malate dehydrogenase, pyruvate,Pi dikinase, and fructose 1,6-bisphosphatase in relation to photosynthetic rate in maize. *Plant Physiol.* **76**, 238–243 (1984).
74. E. Issakidis, M. Lemaire, P. Decottignies, J. P. Jacquot, M. Miginiac-Maslow, Direct evidence for the different roles of the N- and C-terminal regulatory disulfides of sorghum leaf NADP-malate dehydrogenase in its activation by reduced thioredoxin. *FEBS Lett.* **392**, 121–124 (1996).
75. T. P. Howard, M. Metodiev, J. C. Lloyd, C. A. Raines, Thioredoxin-mediated reversible dissociation of a stromal multiprotein complex in response to changes in light availability. *Proc. Natl. Acad. Sci. U.S.A.* **105**, 4056–4061 (2008).
76. A. Yu, Y. Xie, X. Pan, H. Zhang, P. Cao, X. Su, W. Chang, M. Li, Photosynthetic phosphoribulokinase structures: Enzymatic mechanisms and the redox regulation of the Calvin-Benson-Bassham cycle. *Plant Cell* **32**, 1556–1573 (2020).
77. T. P. Howard, J. C. Lloyd, C. A. Raines, Inter-species variation in the oligomeric states of the higher plant Calvin cycle enzymes glyceraldehyde-3-phosphate dehydrogenase and phosphoribulokinase. *J. Exp. Bot.* **62**, 3799–3805 (2011).
78. I. I. Pottosin, G. Schönknecht, Ion channel permeable for divalent and monovalent cations in native spinach thylakoid membranes. *J. Membr. Biol.* **152**, 223–233 (1996).
79. H. Gimmler, G. Schäfer, U. Heber, Low permeability of the chloroplast envelope towards cations. *Proc. 3rd Int. Congr. Photosynth.* (1974).
80. S. Liang, Y. Qi, J. Zhao, Y. Li, R. Wang, J. Shao, X. Liu, L. An, F. Yu, Mutations in the Arabidopsis AtMRS2-11/AtMGT10/VAR5 gene cause leaf reticulation. *Front. Plant Sci.* **8**, 2007 (2017).
81. Y. Sun, R. Yang, L. Li, J. Huang, The magnesium transporter MGT10 is essential for chloroplast development and photosynthesis in *Arabidopsis thaliana*. *Mol. Plant* **10**, 1584–1587 (2017).
82. A. Ikegami, N. Yoshimura, K. Motohashi, S. Takahashi, P. G. N. Romano, T. Hisabori, K. Takamiya, T. Masuda, The CHLI1 subunit of *Arabidopsis thaliana* magnesium chelatase is a target protein of the chloroplast thioredoxin. *J. Biol. Chem.* **282**, 19282–19291 (2007).
83. S. Arrivault, M. Guenther, A. Ivakov, R. Feil, D. Vosloh, J. T. van Dongen, R. Sulpice, M. Stitt, Use of reverse-phase liquid chromatography, linked to tandem mass spectrometry, to profile the Calvin cycle and other metabolic intermediates in Arabidopsis rosettes at different carbon dioxide concentrations. *Plant J. Cell Mol. Biol.* **59**, 826–839 (2009).
84. R. Scheibe, Redox-modulation of chloroplast enzymes: A common principle for individual control. *Plant Physiol.* **96**, 1–3 (1991).

85. C. Swart, S. Martínez-Jaime, M. Gorka, K. Zander, A. Graf, Hit-Gel: Streamlining in-gel protein digestion for high-throughput proteomics experiments. *Sci. Rep.* **8**, 8582 (2018).
86. Y. Perez-Riverol, A. Csordas, J. Bai, M. Bernal-Llinares, S. Hewapathirana, D. J. Kundu, A. Inuganti, J. Griss, G. Mayer, M. Eisenacher, E. Pérez, J. Uszkoreit, J. Pfeuffer, T. Sachsenberg, S. Yilmaz, S. Tiwary, J. Cox, E. Audain, M. Walzer, A. F. Jarnuczak, T. Ternent, A. Brazma, J. A. Vizcaíno, The PRIDE database and related tools and resources in 2019: Improving support for quantification data. *Nucleic Acids Res.* **47**, D442–D450 (2019).
87. M. Van Bel, S. Proost, E. Wischnitzki, S. Movahedi, C. Scheerlinck, Y. Van de Peer, K. Vandepoele, Dissecting plant genomes with the PLAZA comparative genomics platform. *Plant Physiol.* **158**, 590–600 (2012).
88. S. Sato, S. Tabata, H. Hirakawa, E. Asamizu, K. Shirasawa, S. Isobe, T. Kaneko, Y. Nakamura, D. Shibata, K. Aoki, M. Egholm, J. Knight, R. Bogden, C. Li, Y. Shuang, X. Xu, S. Pan, S. Cheng, X. Liu, Y. Ren, J. Wang, A. Albiero, F. Dal Pero, S. Todesco, J. Van Eck, R. M. Buels, A. Bombarely, J. R. Gosselin, M. Huang, J. A. Leto, N. Menda, S. Strickler, L. Mao, S. Gao, I. Y. Tecle, T. York, Y. Zheng, J. T. Vrebalov, J. Lee, S. Zhong, L. A. Mueller, W. J. Stiekema, P. Ribeca, T. Alioto, W. Yang, S. Huang, Y. Du, Z. Zhang, J. Gao, Y. Guo, X. Wang, Y. Li, J. He, C. Li, Z. Cheng, J. Zuo, J. Ren, J. Zhao, L. Yan, H. Jiang, B. Wang, H. Li, Z. Li, F. Fu, B. Chen, B. Han, Q. Feng, D. Fan, Y. Wang, H. Ling, Y. Xue, D. Ware, W. R. McCombie, Z. B. Lippman, J.-M. Chia, K. Jiang, S. Pasternak, L. Gelley, M. Kramer, L. K. Anderson, S.-B. Chang, S. M. Royer, L. A. Shearer, S. M. Stack, J. K. C. Rose, Y. Xu, N. Eannetta, A. J. Matas, R. McQuinn, S. D. Tanksley, F. Camara, R. Guigó, S. Rombauts, J. Fawcett, Y. Van de Peer, D. Zamir, C. Liang, M. Spannagl, H. Gundlach, R. Bruggmann, K. Mayer, Z. Jia, J. Zhang, Z. Ye, G. J. Bishop, S. Butcher, R. Lopez-Cobollo, D. Buchan, I. Filippis, J. Abbott, R. Dixit, M. Singh, A. Singh, J. K. Pal, A. Pandit, P. K. Singh, A. K. Mahato, V. Dogra, K. Gaikwad, T. R. Sharma, T. Mohapatra, N. K. Singh, M. Causse, C. Rothan, T. Schiex, C. Noirot, A. Bellec, C. Klopp, C. Delalande, H. Berges, J. Mariette, P. Frasse, S. Vautrin, M. Zouine, A. Latché, C. Rousseau, F. Regad, J.-C. Pech, M. Philippot, M. Bouzayen, P. Pericard, S. Osorio, A. F. del Carmen, A. Monforte, A. Granell, R. Fernandez-Muñoz, M. Conte, G. Lichtenstein, F. Carrari, G. De Bellis, F. Fuligni, C. Peano, S. Grandillo, P. Termolino, M. Pietrella, E. Fantini, G. Falcone, A. Fiore, G. Giuliano, L. Lopez, P. Facella, G. Perrotta, L. Daddiego, G. Bryan, M. Orozco, X. Pastor, D. Torrents, M. G. M. van Schriek, R. M. C. Feron, J. van Oeveren, P. de Heer, L. daPonte, S. Jacobs-Oomen, M. Cariaso, M. Prins, M. J. T. van Eijk, A. Janssen, M. J. J. van Haaren, S.-H. Jo, J. Kim, S.-Y. Kwon, S. Kim, D.-H. Koo, S. Lee, C.-G. Hur, C. Clouser, A. Rico, A. Hallab, C. Gebhardt, K. Klee, A. Jöcker, J. Warfsmann, U. Göbel, S. Kawamura, K. Yano, J. D. Sherman, H. Fukuoka, S. Negoro, S. Bhutty, P. Chowdhury, D. Chattopadhyay, E. Datema, S. Smit, E. G. W. M. Schijlen, J. van de Belt, J. C. van Haarst, S. A. Peters, M. J. van Staveren, M. H. C. Henkens, P. J. W. Mooyman, T. Hesselink, R. C. H. J. van Ham, G. Jiang, M. Droege, D. Choi, B.-C. Kang, B. D. Kim, M. Park, S. Kim, S.-I. Yeom, Y.-H. Lee, Y.-D. Choi, G. Li, J. Gao, Y. Liu, S. Huang, V. Fernandez-Pedrosa, C. Collado, S. Zuñiga, G. Wang, R. Cade, R. A. Dietrich, J. Rogers, S. Knapp, Z. Fei, R. A. White, T. W. Thannhauser, J. J. Giovannoni, M. A. Botella, L. Gilbert, R. Gonzalez, The tomato genome sequence provides insights into fleshy fruit evolution. *Nature* **485**, 635–641 (2012).
89. X. Wang, H. Wang, J. Wang, R. Sun, J. Wu, S. Liu, Y. Bai, J.-H. Mun, I. Bancroft, F. Cheng, S. Huang, X. Li, W. Hua, J. Wang, X. Wang, M. Freeling, J. C. Pires, A. H. Paterson, B. Chalhoub, B. Wang, A. Hayward, A. G. Sharpe, B.-S. Park, B. Weisshaar, B. Liu, B. Li, B. Liu, C. Tong, C. Song, C. Duran, C. Peng, C. Geng, C. Koh, C. Lin, D. Edwards, D. Mu, D. Shen, E. Soumpourou, F. Li, F. Fraser, G. Conant, G. Lassalle, G. J. King, G. Bonnema, H. Tang, H. Wang, H. Belcram, H. Zhou, H. Hirakawa, H. Abe, H. Guo, H. Wang, H. Jin, I. A. P. Parkin, J. Batley, J.-S. Kim, J. Just, J. Li, J. Xu, J. Deng, J. A. Kim, J. Li, J. Yu, J. Meng, J. Wang, J. Min, J. Poulain, J. Wang, K. Hatakeyama, K. Wu, L. Wang, L. Fang, M. Trick, M. G. Links, M. Zhao, M. Jin, N. Ramchiary, N. Drou, P. J. Berkman, Q. Cai, Q. Huang, R. Li, S. Tabata, S. Cheng, S. Zhang, S. Zhang, S. Huang, S. Sato, S. Sun, S.-J. Kwon, S.-R. Choi, T.-H. Lee, W. Fan, X. Zhao, X. Tan, X. Xu, Y. Wang, Y. Qiu, Y. Yin, Y. Li, Y. Du, Y. Liao, Y. Lim, Y. Narusaka, Y. Wang, Z. Wang, Z. Li, Z. Wang, Z. Xiong, Z. Zhang, The genome of the mesopolyploid crop species *Brassica rapa*. *Nat. Genet.* **43**, 1035–1039 (2011).
90. X. Xu, S. Pan, S. Cheng, B. Zhang, D. Mu, P. Ni, G. Zhang, S. Yang, R. Li, J. Wang, G. Orjeda, F. Guzman, M. Torres, R. Lozano, O. Ponce, D. Martinez, G. De la Cruz, S. K. Chakrabarti, V. U. Patil, K. G. Skryabin, B. B. Kuznetsov, N. V. Ravin, T. V. Kolganova, A. V. Beletsky, A. V. Mardanov, A. Di Genova, D. M. Bolser, D. M. A. Martin, G. Li, Y. Yang, H. Kuang, Q. Hu, X. Xiong, G. J. Bishop, B. Sagredo, N. Mejía, W. Zagorski, R. Gromadka, J. Gawor, P. Szczesny, S. Huang, Z. Zhang, C. Liang, J. He, Y. Li, Y. He, J. Xu, Y. Zhang, B. Xie, Y. Du, D. Qu, M. Bonierbale, M. Ghislain, M. del Rosario Herrera, G. Giuliano, M. Pietrella, G. Perrotta, P. Facella, K. O'Brien, S. E. Feingold, L. E. Barreiro, G. A. Massa, L. Diambra, B. R. Whitty, B. Vaillancourt, H. Lin, A. N. Massa, M. Geoffroy, S. Lundback, D. DellaPenna, C. R. Buell, S. K. Sharma, D. F. Marshall, R. Waugh, G. J. Bryan, M. Destefanis, I. Nagy, D. Milbourne, S. J. Thomson, M. Fiers, J. M. E. Jacobs, K. L. Nielsen, M. Sønderkær, M. Iovene, G. A. Torres, J. Jiang, R. E. Veilleux, C. W. B. Bachem, J. de Boer, T. Borm, B. Kloosterman, H. van Eck, E. Datema, B. te Lintel Hekkert, A. Goverse, R. C. H. J. van Ham, R. G. F. Visser, Genome sequence and analysis of the tuber crop potato. *Nature* **475**, 189–195 (2011).
91. C. Camacho, G. Coulouris, V. Avagyan, N. Ma, J. Papadopoulos, K. Bealer, T. L. Madden, BLAST+: Architecture and applications. *BMC Bioinformatics* **10**, 421 (2009).
92. A. J. Enright, S. Van Dongen, C. A. Ouzounis, An efficient algorithm for large-scale detection of protein families. *Nucleic Acids Res.* **30**, 1575–1584 (2002).
93. L. Li, C. J. Stoeckert, D. S. Roos, OrthoMCL: Identification of ortholog groups for eukaryotic genomes. *Genome Res.* **13**, 2178–2189 (2003).
94. N. Sierro, J. N. D. Battey, S. Ouadi, L. Bovet, S. Goepfert, N. Bakaher, M. C. Peitsch, N. V. Ivanov, Reference genomes and transcriptomes of *Nicotiana sylvestris* and *Nicotiana tomentosiformis*. *Genome Biol.* **14**, R60 (2013).
95. M. Van Bel, S. Proost, C. Van Neste, D. Deforce, Y. Van de Peer, K. Vandepoele, TRAPID: An efficient online tool for the functional and comparative analysis of de novo RNA-Seq transcriptomes. *Genome Biol.* **14**, R134 (2013).
96. J. C. Moreno, S. Martínez-Jaime, J. Schwartzmann, D. Karcher, M. Tillich, A. Graf, R. Bock, Temporal proteomics of inducible RNAi lines of Clp protease subunits identifies putative protease substrates. *Plant Physiol.* **176**, 1485–1508 (2018).
97. J. Cox, M. Mann, MaxQuant enables high peptide identification rates, individualized p.p.b.-range mass accuracies and proteome-wide protein quantification. *Nat. Biotechnol.* **26**, 1367–1372 (2008).
98. A. P. Hertle, T. Blunder, T. Wunder, P. Pesaresi, M. Pribil, U. Armbruster, D. Leister, PGRL1 is the elusive ferredoxin-plastoquinone reductase in photosynthetic cyclic electron flow. *Mol. Cell* **49**, 511–523 (2013).
99. M. Stitt, R. Ellison, R. Sulpice, Y. Gibon, A. Whitwell, R. Skilbeck, S. Parker, Cryogenic grinder system. *Vol Ger. Pat. No 081460025U1 MPGSFX Link Resolv.* (2007).
100. S. Arrivault, M. Guenther, S. C. Fry, M. M. F. F. Fuenfgeld, D. Veyel, T. Mettler-Altmann, M. Stitt, J. E. Lunn, Synthesis and use of stable-isotope-labeled internal standards for quantification of phosphorylated metabolites by LC-MS/MS. *Anal. Chem.* **87**, 6896–6904 (2015).
101. L. Merlo, P. Geigenberger, M. Hajirezaei, M. Stitt, Changes of carbohydrates, metabolites and enzyme activities in potato tubers during development, and within a single tuber along a stolon-apex gradient. *J. Plant Physiol.* **142**, 392–402 (1993).
102. H. Winter, D. G. Robinson, H. W. Heldt, Subcellular volumes and metabolite concentrations in spinach leaves. *Planta* **193**, 530–535 (1994).
103. M. Szecowka, R. Heise, T. Tohge, A. Nunes-Nesi, D. Vosloh, J. Huege, R. Feil, J. Lunn, Z. Nikoloski, M. Stitt, A. R. Fernie, S. Arrivault, Metabolic fluxes in an illuminated Arabidopsis rosette. *Plant Cell* **25**, 694–714 (2013).
104. F. Cadet, J. C. Meunier, pH and kinetic studies of chloroplast sedoheptulose-1,7-bisphosphatase from spinach (*Spinacia oleracea*). *Biochem. J.* **253**, 249–254 (1988).
105. B. Surek, A. Heilbronn, A. Austen, E. Latzko, Purification and characterization of phosphoribulokinase from wheat leaves. *Planta* **165**, 507–512 (1985).
106. H. K. Brandes, F. C. Hartman, T. Y. Lu, F. W. Larimer, Efficient expression of the gene for spinach phosphoribulokinase in *Pichia pastoris* and utilization of the recombinant enzyme to explore the role of regulatory cysteinyl residues by site-directed mutagenesis. *J. Biol. Chem.* **271**, 6490–6496 (1996).
107. N. R. Baker, Chlorophyll fluorescence: A probe of photosynthesis *in vivo*. *Annu. Rev. Plant Biol.* **59**, 89–113 (2008).
108. A. Roy, A. Kucukural, Y. Zhang, I-TASSER: A unified platform for automated protein structure and function prediction. *Nat. Protoc.* **5**, 725–738 (2010).
109. K. Katoh, D. M. Standley, MAFFT multiple sequence alignment software version 7: Improvements in performance and usability. *Mol. Biol. Evol.* **30**, 772–780 (2013).
110. F. Sparla, P. Pupillo, P. Trost, The C-terminal extension of glyceraldehyde-3-phosphate dehydrogenase subunit B acts as an autoinhibitory domain regulated by thioredoxins and nicotinamide adenine dinucleotide. *J. Biol. Chem.* **277**, 44946–44952 (2002).
111. G. Wu, G. Ortiz-Flores, A. Ortiz-Lopez, D. R. Ort, A point mutation in atpC1 raises the redox potential of the Arabidopsis chloroplast ATP synthase γ-subunit regulatory disulfide above the range of thioredoxin modulation. *J. Biol. Chem.* **282**, 36782–36789 (2007).
112. Y. Meyer, C. Riondet, L. Constans, M. R. Abdelgawwad, J. P. Reichheld, F. Vignols, Evolution of redoxin genes in the green lineage. *Photosynth. Res.* **89**, 179–192 (2006).
113. M. Broin, S. Cuiné, F. Eymery, P. Rey, The plastidic 2-cysteine peroxiredoxin is a target for a thioredoxin involved in the protection of the photosynthetic apparatus against oxidative damage. *Plant Cell* **14**, 1417–1432 (2002).
114. C. Marchand, P. Le Maréchal, Y. Meyer, M. Miginiac-Maslow, E. Issakidis-Bourguet, P. Decottignies, New targets of Arabidopsis thioredoxins revealed by proteomic analysis. *Proteomics* **4**, 2696–2706 (2004).
115. D. Yamazaki, K. Motohashi, T. Kasama, Y. Hara, T. Hisabori, Target proteins of the cytosolic thioredoxins in *Arabidopsis thaliana*. *Plant Cell Physiol.* **45**, 18–27 (2004).
116. D. P. Dixon, M. Skipsey, N. M. Grundy, R. Edwards, Stress-induced protein S-glutathionylation in Arabidopsis. *Plant Physiol.* **138**, 2233–2244 (2005).
117. C. Lindermayr, G. Saalbach, J. Durner, Proteomic identification of S-nitrosylated proteins in Arabidopsis. *Plant Physiol.* **137**, 921–930 (2005).

118. N. Rouhier, A. Villarejo, M. Srivastava, E. Gelhaye, O. Keech, M. Droux, I. Finkemeier, G. Samuelsson, K. J. Dietz, J.-P. Jacquot, G. Wingsle, Identification of plant glutaredoxin targets. *Antioxid. Redox Signal.* **7**, 919–929 (2005).
119. C. Marchand, P. Le Maréchal, Y. Meyer, P. Decottignies, Comparative proteomic approaches for the isolation of proteins interacting with thioredoxin. *Proteomics* **6**, 6528–6537 (2006).
120. K. Motohashi, T. Hisabori, HCF164 receives reducing equivalents from stromal thioredoxin across the thylakoid membrane and mediates reduction of target proteins in the thylakoid lumen. *J. Biol. Chem.* **281**, 35039–35047 (2006).
121. A. M. Winger, N. L. Taylor, J. L. Heazlewood, D. A. Day, A. H. Millar, Identification of intra- and intermolecular disulphide bonding in the plant mitochondrial proteome by diagonal gel electrophoresis. *Proteomics* **7**, 4158–4170 (2007).
122. M. C. Romero-Puertas, N. Campostrini, A. Mattè, P. G. Righetti, M. Perazzolli, L. Zolla, P. Roepstorff, M. Delledonne, Proteomic analysis of S-nitrosylated proteins in *Arabidopsis thaliana* undergoing hypersensitive response. *Proteomics* **8**, 1459–1469 (2008).
123. E. Ströher, K.-J. Dietz, The dynamic thiol-disulphide redox proteome of the *Arabidopsis thaliana* chloroplast as revealed by differential electrophoretic mobility. *Physiol. Plant.* **133**, 566–583 (2008).
124. S. Alvarez, G. H. Wilson, S. Chen, Determination of *in vivo* disulfide-bonded proteins in Arabidopsis. *J. Chromatogr. B Anal. Technol. Biomed. Life Sci.* **877**, 101–104 (2009).
125. S. Alvarez, M. Zhu, S. Chen, Proteomics of Arabidopsis redox proteins in response to methyl jasmonate. *J. Proteome* **73**, 30–40 (2009).
126. M. Hall, A. Mata-Cabana, H.-E. Akerlund, F. J. Florencio, W. P. Schröder, M. Lindahl, T. Kieselbach, Thioredoxin targets of the plant chloroplast lumen and their implications for plastid function. *Proteomics* **10**, 987–1001 (2010).
127. C. H. Marchand, H. Vanacker, V. Collin, E. Issakidis-Bourguet, P. L. Maréchal, P. Decottignies, Thioredoxin targets in Arabidopsis roots. *Proteomics* **10**, 2418–2428 (2010).
128. M. C. Palmieri, C. Lindermayr, H. Bauwe, C. Steinhauser, J. Durner, Regulation of plant glycine decarboxylase by S-nitrosylation and glutathionylation. *Plant Physiol.* **152**, 1514–1528 (2010).
129. A. Fares, M. Rossignol, J.-B. Peltier, Proteomics investigation of endogenous S-nitrosylation in Arabidopsis. *Biochem. Biophys. Res. Commun.* **416**, 331–336 (2011).
130. H. Wang, S. Wang, Y. Lu, S. Alvarez, L. M. Hicks, X. Ge, Y. Xia, Proteomic analysis of early-responsive redox-sensitive proteins in Arabidopsis. *J. Proteome Res.* **11**, 412–424 (2012).
131. M. Muthuramalingam, A. Matros, R. Scheibe, H.-P. Mock, K.-J. Dietz, The hydrogen peroxide-sensitive proteome of the chloroplast *in vitro* and *in vivo*. *Front. Plant Sci.* **4**, 54 (2013).
132. K. Yoshida, K. Noguchi, K. Motohashi, T. Hisabori, Systematic exploration of thioredoxin target proteins in plant mitochondria. *Plant Cell Physiol.* **54**, 875–892 (2013).
133. P. Liu, H. Zhang, H. Wang, Y. Xia, Identification of redox-sensitive cysteines in the Arabidopsis proteome using OxiTRAQ, a quantitative redox proteomics method. *Proteomics* **14**, 750–762 (2014).
134. Y. Lu, J.-J. Du, Z.-B. Yu, J.-J. Peng, J.-N. Xu, X.-Y. Wang, Identification of potential targets for thylakoid oxidoreductase AtVKOR/LTO1 in chloroplasts. *Protein Pept. Lett.* **22**, 219–225 (2014).
135. J. Puyaubert, A. Fares, N. Rézé, J.-B. Peltier, E. Baudouin, Identification of endogenously S-nitrosylated proteins in Arabidopsis plantlets: Effect of cold stress on cysteine nitrosylation level. *Plant Sci. Int. J. Exp. Plant Biol.* **215-216**, 150–156 (2014).
136. C. Waszczak, S. Akter, D. Eeckhout, G. Persiau, K. Wahni, N. Bodra, I. Van Molle, B. De Smet, D. Vertommen, K. Gevaert, G. De Jaeger, M. Van Montagu, J. Messens, F. Van Breusegem, Sulfenome mining in *Arabidopsis thaliana*. *Proc. Natl. Acad. Sci. U.S.A.* **111**, 11545–11550 (2014).
137. S. Akter, J. Huang, N. Bodra, B. De Smet, K. Wahni, D. Rombaut, J. Pauwels, K. Gevaert, K. Carroll, F. Van Breusegem, J. Messens, DYn-2 based identification of Arabidopsis sulfenomes. *Mol. Cell. Proteomics MCP* **14**, 1183–1200 (2015).
138. Á. Aroca, A. Serna, C. Gotor, L. C. Romero, S-sulfhydration: A cysteine posttranslational modification in plant systems. *Plant Physiol.* **168**, 334–342 (2015).
139. J. Hu, X. Huang, L. Chen, X. Sun, C. Lu, L. Zhang, Y. Wang, J. Zuo, Site-specific nitrosoproteomic identification of endogenously S-nitrosylated proteins in Arabidopsis. *Plant Physiol.* **167**, 1731–1746 (2015).
140. P. Liu, H. Zhang, B. Yu, L. Xiong, Y. Xia, Proteomic identification of early salicylate- and flg22-responsive redox-sensitive proteins in Arabidopsis. *Sci. Rep.* **5**, 8625 (2015).
141. W. O. Slade, E. G. Werth, E. W. McConnell, S. Alvarez, L. M. Hicks, Quantifying reversible oxidation of protein thiols in photosynthetic organisms. *J. Am. Soc. Mass Spectrom.* **26**, 631–640 (2015).
142. D. Cerveau, A. Kraut, H. U. Stotz, M. J. Mueller, Y. Couté, P. Rey, Characterization of the Arabidopsis thaliana 2-Cys peroxiredoxin interactome. *Plant Sci. Int. J. Exp. Plant Biol.* **252**, 30–41 (2016).
143. A. Aroca, J. M. Benito, C. Gotor, L. C. Romero, Persulfidation proteome reveals the regulation of protein function by hydrogen sulfide in diverse biological processes in Arabidopsis. *J. Exp. Bot.* **68**, 4915–4927 (2017).
144. Z. Yin, K. Balmant, S. Geng, N. Zhu, T. Zhang, C. Dufresne, S. Dai, S. Chen, Bicarbonate induced redox proteome changes in Arabidopsis suspension cells. *Front. Plant Sci.* **8**, 58 (2017).
145. B. D. Smet, P. Willems, A. D. Fernandez-Fernandez, S. Alseekh, A. R. Fernie, J. Messens, F. V. Breusegem, In vivo detection of protein cysteine sulfenylation in plastids. *Plant J.* **97**, 765–778 (2019).
146. M. González, V. Delgado-Requerey, J. Ferrández, A. Serna, F. J. Cejudo, Insights into the function of NADPH thioredoxin reductase C (NTRC) based on identification of NTRC-interacting proteins *in vivo*. *J. Exp. Bot.* **70**, 5787–5798 (2019).
147. J. Huang, P. Willems, B. Wei, C. Tian, R. B. Ferreira, N. Bodra, S. A. Martínez Gache, K. Wahni, K. Liu, D. Vertommen, K. Gevaert, K. S. Carroll, M. Van Montagu, J. Yang, F. Van Breusegem, J. Messens, Mining for protein S-sulfenylation in Arabidopsis uncovers redox-sensitive sites. *Proc. Natl. Acad. Sci. U.S.A.* **116**, 21256–21261 (2019).

Acknowledgments: We thank B. Hausmann and H. Kulka for plant cultivation; G. Wittenberg, S. Lange, and A. Coutant for assistance in harvesting samples; C. Raines for her gift of the anti-cpFBPase antibody; O. Vallon for help with data mining in the SRA database; A. Küken, K. Wostrikoff, B. Bailleul, P. Joliot, O. Vallon, I. Lafontaine, S. Lemaire, J. Henri, and P. Crozet for fruitful discussions; and T. Armarego-Marriott, A. Falciatore, and F.-A. Wollman for critical reading of the manuscript. **Funding:** This work was supported by Max Planck Society, Germany; Centre National de la Recherche Scientifique, France; Sorbonne Université, France; German Research Foundation grant TRR 175/D02 (to T.M.); German Research Foundation grants FOR 804, BO 1482/15-2, FOR 2092, and BO 1482/17-1 (to R.B.); German Research Foundation grant TI 605/5-1 (to M.T.); French National Research Agency grant LabEx Dynamo ANR-LABX-011 (UMR7141); and European Union's Horizon 2020 research and innovation programme grant 862201 (to Z.N.) (this publication reflects only the author's view and the Commission is not responsible for any use that may be made of the information it contains).
Author contributions: A.B. and A.G. conceived the redox proteomics experiment, which was performed by A.B. and C.S. S.A. and A.B. performed the metabolomics experiments. M.T., S.P., and A.B. created the tobacco redox proteomic database. D.Z., A.B., and T.M. conceived and performed the method for redox proteomics data analysis. A.B. and Z.N. discussed calculations for *Ea* and metabolomic data. R.B., T.M., and M.T. acquired funding. A.B., D.Z., M.T., S.P., and T.M. wrote the original draft of the paper, which was reviewed and edited by M.S., R.B., Z.N., S.A., A.B., D.Z., and T.M. **Competing interests:** The authors declare that they have no competing interests. **Data and materials availability:** All data needed to evaluate the conclusions in the paper are present in the paper and/or the Supplementary Materials. Additional data related to this paper is available on https://www.ebi.ac.uk/pride/ with the dataset identifier PXD025217 for proteomics data

Submitted 2 April 2021
Accepted 3 November 2021
Published 17 December 2021
10.1126/sciadv.abi8307

ScienceAdvances

Topology of the redox network during induction of photosynthesis as revealed by time-resolved proteomics in tobacco

David ZimmerCorné SwartAlexander GrafStéphanie ArrivaultMichael TillichSebastian ProostZoran NikoloskiMark StittRalph BockTimo MühlhausAlix Boulouis

Sci. Adv., 7 (51), eabi8307. • DOI: 10.1126/sciadv.abi8307

Science Advances (ISSN) is published by the American Association for the Advancement of Science. 1200 New York Avenue NW, Washington, DC 20005. The title *Science Advances* is a registered trademark of AAAS.